Research Article | Vol. 32, No. 22 / 21 Oct 2024 / Optics Express 39685
Optics EXPRESS

Asynchronous visible light communication and positioning system based on a multi-carrier orthogonal coding mechanism

ZHONGXU LIU,[1] DAWEI XIE,[1] XIAODI YOU,[2] AND CHANGYUAN YU[1,*]

[1]Department of Electrical and Electronic Engineering, The Hong Kong Polytechnic University, Kowloon, Hong Kong SAR 999077, China
[2]School of Electronic and Information Engineering, Soochow University, Suzhou 215000, China
*changyuan.yu@polyu.edu.hk

Abstract: This paper presents an asynchronous visible light communication and positioning (VLCP) system leveraging the multi-carrier orthogonal coding mechanism (MC-OCM) based on complete complementary (CC) codes. Utilizing the superior correlation properties of CC codes, our system first achieves interference-free transmission from multiple access interference and inter-symbol interference, thus simultaneously enhancing the accuracy of data transmission and receiver location in asynchronous code division multiplexing-based VLCP systems. Numerical results confirm the proposed VLCP system's superiority, featuring an average BER below the FEC standard and an average PE less than 3 cm in challenging system settings with asynchronous transmission and multipath propagation.

© 2024 Optica Publishing Group under the terms of the Optica Open Access Publishing Agreement

1. Introduction

With the advent of 5 G and the impending demands of 6 G networks, the limitations of traditional radio frequency (RF) communication systems have become increasingly apparent, particularly in terms of spectrum congestion and susceptibility to electromagnetic interference [1–3]. To address these challenges, visible light communication (VLC) has emerged as a promising alternative, leveraging the vast and unregulated visible light spectrum (430 THz to 790 THz) to deliver high-speed, low-latency data transmission [4]. Concurrently, visible light positioning (VLP) has gained attention for its potential to provide precise indoor localization using existing lighting infrastructure [5]. By integrating VLC and VLP into a unified system, significant synergies can be achieved, enhancing both communication and positioning capabilities. This integration, referred to as visible light communication and positioning (VLCP), offers numerous advantages, such as maximizing the utilization of existing LED lighting infrastructure, reducing electromagnetic interference, and enhancing system efficiency and user experience [6,7]. Such a system is particularly suited for high-precision and reliable applications, including smart homes, healthcare, augmented reality, and industrial automation.

Although VLC and VLP operate in the same visible light spectrum and typically use light-emitting diodes (LEDs) as transmitters and photodetector (PD) as the receiver, they handle received signals differently. Specifically, VLC directly recovers communication data from the received signal, while VLP first extracts received signal strength (RSS), time of arrival (TOA), or angle of arrival (AOA) information from the received signal and then uses trilateration algorithms to estimate positional information [8]. Among the methods used in VLP systems, RSS combined with the trilateration algorithm is widely studied due to its simple principle, economic efficiency, and minimal hardware complexity [9,10]. However, these VLP systems typically require multiple transmitters to broadcast different positioning information. Thus, integrating VLC and VLP within a unified VLCP framework requires strategies to not only simultaneously transmit VLC and

#537793 https://doi.org/10.1364/OE.537793
Journal © 2024 Received 8 Aug 2024; revised 5 Sep 2024; accepted 18 Sep 2024; published 16 Oct 2024

© 2024 Optica Publishing Group under the terms of the Open Access Publishing Agreement. Users may use, reuse, and build upon the article, or use the article for text or data mining, so long as such uses are for non-commercial purposes and appropriate attribution is maintained. All other rights are reserved.

Optics EXPRESS

VLP information but also to prevent signal interference between different transmitters. To achieve this, VLCP systems often employ multiplexing techniques such as time division multiplexing (TDM), frequency division multiplexing (FDM), or code division multiplexing (CDM).

In TDM-based VLCP systems, VLC and VLP signals are transmitted during non-overlapping time intervals to prevent interference, requiring precise time synchronization between multiple transmitters and receivers [11–13]. However, as the number of supported users increases, communication and positioning delays become more severe. Conversely, FDM-based VLCP systems divide the total spectrum into separate parts for VLC and VLP information [14–17], but they suffer from high out-of-band interference (OOBI) and peak-to-average power ratio (PAPR), which inevitably degrade system performance. Although filter bank multicarrier-based subcarrier multiplexing (FBMC-SCM) was used to reduce the OOBI, it still needs additional guard bands to prevent interference between sub-bands [18,19]. Furthermore, TDM or FDM architectures require additional time or spectrum resources for VLP signals, limiting the efficient utilization of transmission resources for VLC. To address these limitations, CDM-based VLCP systems offer a more innovative solution. These systems employ orthogonal coding mechanisms to distinguish different VLCP signals, allowing VLC and VLP information to coexist within the same spectrum and time slots without mutual interference [20,21]. This significantly enhances resource utilization efficiency and reduces signal distortion and power consumption requirements due to lower PAPR characteristics [22,23]. However, CDM-based VLCP systems rely on the correlation properties of codewords to maintain orthogonality among VLCP signals, which requires codewords to demonstrate negligible cross-correlation and pronounced auto-correlation. Various codeword options have been explored, including random optical codes [24] and optical orthogonal codes [25] applied in CDM-based VLC systems, and pseudorandom (PN) sequences [26] and Walsh codes [27] used in CDM-based VLP systems. However, a core requirement for such systems is maintaining strict system synchronization, which remains challenging due to non-ideal clock precision [20] and multipath effect [28]. In practice, asynchronous transmission and multipath propagation always result in chip offset at the receiver, disrupting the orthogonality of the encoded signals and inducing both multiple access interference (MAI) and inter-symbol interference (ISI). Experimental studies have shown significant degradation in VLP performance under the influence of MAI caused by asynchronous transmission [29].

To mitigate MAI and ISI in VLCP systems, Chen et al. developed zero correlation zone (ZCZ) codes, demonstrating superior performance over zero cross-correlation (ZCC) and Walsh codes in quasi-synchronous systems [20,23]. However, ZCZ codes' orthogonality is confined to a specific chip offset range, resulting in their ineffectiveness in eliminating MAI and ISI in asynchronous systems. Tawfiq et al. proposed cyclic orthogonal Walsh-Hadamard (COWH) codes designed to preserve orthogonality regardless of chip offset, but their poor autocorrelation properties make them less adaptable to multipath propagation environments [30]. It is noteworthy that both ZCZ and COWH codes maintain their correlation characteristics optimally when handling single bitstream transmissions. However, continuous bitstream transmission introduces complexities that interactions between adjacent bits can distort these codes' correlation properties, affecting system performance. Thus, to the best of our knowledge, no existing research has effectively addressed the mitigation of MAI and ISI in asynchronous CDM-based VLCP systems. Given these challenges, there is an urgent need to develop innovative coding schemes, especially designed for asynchronous operational environments. These strategies must inherently decrease the VLCP system's reliance on precise synchronization, enhancing system resilience and performance. Achieving this necessitates the development of codewords that can keep robust correlation properties under asynchronous conditions and during continuous bitstream transmission, effectively addressing the complexities and challenges of real-world information transmission.

Optics EXPRESS

In this paper, we present an innovative asynchronous VLCP system design based on a multi-carrier orthogonal coding mechanism (MC-OCM). The proposed method overcomes the traditional dependency on synchronization and first realizes MAI and ISI-free transmission in asynchronous CDM-based VLCP systems. We leverage complete complementary (CC) codes, renowned for their superior cross-correlation and auto-correlation properties in radio frequency wireless communication, even in asynchronous transmission scenarios [31,32]. This feature is pivotal for maintaining the orthogonality of VLCP signals amidst asynchronous transmissions. Unlike single sub-codes like ZCZ codes or COWH codes, each CC code comprises multiple sub-codes that need to be transmitted through independent channels. To facilitate this, we design a multi-carrier transmission mechanism, including dedicated encoders and decoders, to ensure simultaneous and efficient transmission of each CC sub-code. Thanks to the perfect correlation properties of CC codes, our system effectively suppresses MAI and ISI caused by asynchronous transmission and multipath propagation. This enables the receiver to precisely decode VLCP signals from various LEDs and extract the correlation values associated with each VLCP signal and local reference codewords. Applying a threshold to these values facilitates the recovery of user data for the VLC function. Moreover, calculating the received signal strength (RSS) based on these values for each VLCP signal allows for the deployment of trilateration algorithms to locate the receiver for the VLP function. Thus, our system concurrently supports VLC and VLP functionalities without strict synchronization requirements. Theoretical analysis validates that our proposed VLCP system fundamentally eliminates MAI and ISI issues caused by asynchronous transmission and multipath propagation. Simulation results successfully confirm the superiority of the CC code-based VLCP system over ZCZ and COWH code counterparts. Especially in challenging scenarios featuring asynchronous and continuous bitstream transmission and multipath propagation, our proposed system reduces the average BER by approximately 99% and 98% and the average PE by about 96% and 92%, compared to ZCZ and COWH codes-based VLCP systems, respectively.

The remainder of this paper is structured as follows: Section 2 analyzes the correlation properties necessary for codewords to maintain orthogonality in both synchronous and asynchronous VLCP systems. Then, Section 3 introduces the generation method for CC codes and analyzes their unique correlation properties. Following this, Section 4 discusses the working principles and simulation setup of the proposed VLCP system based on MC-OCM. Next, Section 5 presents a comparative analysis of the impact of different coding schemes on the performance of the VLCP system across various scenarios. Finally, Section 6 summarizes the main contribution of this work.

2. Analysis of correlation properties of codewords used in VLCP systems

First, we outline the requirements for the correlation properties of codewords employed in both synchronous and asynchronous CDM-based VLCP systems. Figure 1 illustrates a schematic depiction of the correlation between the received signal and the local reference codeword. Here, the received signal contains CDM-based VLCP signals from two independent LED transmitters. Notably, within a synchronized system framework, the specifics of correlation operations are largely unaffected, whether the transmission involves a single bitstream or continuous bitstream.

In CDM-based VLCP systems, the orthogonality of signals is essential to avoid interference among VLCP signals and facilitate their precise identification by the receiver, which directly relies on the correlation properties of the codeword. For synchronous transmission with a single or continuous bitstream, codewords should exhibit minimal cross-correlation (CCF) to minimize interference and have a sharp auto-correlation function (ACF) to assist signal identification. As for asynchronous scenarios with single bitstream transmission, given the potential for chip misalignment, the codewords need enhanced correlation properties that are zero periodic cross-correlation functions (PCCFs) for all possible chip offsets and peak periodic auto-correlation

Optics EXPRESS

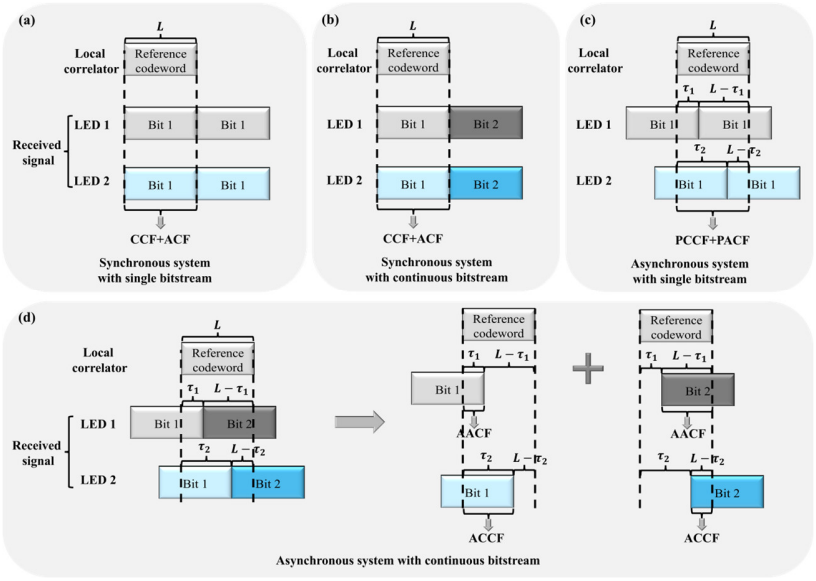

Fig. 1. Schematic diagram of the correlation between local reference codeword and received VLCP signals in (a) the synchronous system with single bitstream; (b) the synchronous system with continuous bitstream; (c) the asynchronous system with single bitstream; and (d) the asynchronous system with continuous bitstream, where the local correlator contains the codeword for LED 1. The bitstream patterns of LED 1 and LED 2 illustrate the scenarios where the VLCP signals transmitted by these two transmitters arrive at the receiver after experiencing different time delays (denoted as τ), and L denotes the length of codewords.

functions (PACFs) exclusively at zero offset. This ensures sustained orthogonality among encoded VLCP signals, regardless of any time delay. Moreover, to sustain this orthogonality in an asynchronous system with continuous bitstream transmission, codewords' correlation properties must follow stricter criteria. As illustrated in Fig. 1(c), when adjacent bits carry different information, the correlation values between the reference codeword and the received signal can be construed as the summation of multiple aperiodic cross-correlation functions (AACFs) and aperiodic auto-correlation functions (ACCFs). Thus, codewords must not only satisfy the periodic correlation properties but also feature ACCFs nearing zero for all possible chip offsets and AACFs peaking at zero chip offset. This ensures that VLCP signals encoded with these codewords can be differentiated from others at any time delay while maintaining accurate self-recognition. In light of these considerations, we introduce the employment of CC codes, distinguished by their superior correlation properties, to establish the VLCP system. The subsequent section delves into the construction and correlation properties of CC codes.

3. Construction and correlation properties of CC codes

3.1. Generation of CC codes

We begin by introducing the construction process of CC codes. Let $\boldsymbol{A}$ be an N-dimensional Walsh-Hadamard matrix consisting of elements a_{ij}, which is:

Optics EXPRESS

$$\boldsymbol{A} = \begin{bmatrix} \boldsymbol{A}_1 \\ \boldsymbol{A}_2 \\ \vdots \\ \boldsymbol{A}_N \end{bmatrix} = \begin{bmatrix} a_{11} & a_{12} & \cdots & a_{1N} \\ a_{21} & a_{22} & \cdots & a_{2N} \\ \vdots & \vdots & \vdots & \vdots \\ a_{N1} & a_{N2} & \cdots & a_{NN} \end{bmatrix}, \tag{1}$$

and let $\boldsymbol{B}$ be another N-dimensional Walsh-Hadamard matrix, which is:

$$\boldsymbol{B} = \begin{bmatrix} b_{11} & b_{12} & \cdots & b_{1N} \\ b_{21} & b_{22} & \cdots & b_{2N} \\ \vdots & \vdots & \vdots & \vdots \\ b_{N1} & b_{N2} & \cdots & b_{NN} \end{bmatrix}. \tag{2}$$

Then, based on matrices $\boldsymbol{A}$ and $\boldsymbol{B}$, we can generate a set of N sequences of length N^2 as:

$$\begin{cases} \boldsymbol{C}_1 = (b_{11}\boldsymbol{A}_1 \quad b_{12}\boldsymbol{A}_2 \quad \cdots \quad b_{1N}\boldsymbol{A}_N) = \left(c_{11}, \quad c_{12}, \quad \cdots \quad c_{1N^2} \right) \\ \boldsymbol{C}_2 = (b_{21}\boldsymbol{A}_1 \quad b_{22}\boldsymbol{A}_2 \quad \cdots \quad b_{2N}\boldsymbol{A}_N) = \left(c_{21}, \quad c_{22}, \quad \cdots \quad c_{2N^2} \right) \\ \vdots = \quad \vdots \quad \vdots \quad \vdots \quad \vdots \quad \vdots \\ \boldsymbol{C}_N = (b_{N1}\boldsymbol{A}_1 \quad b_{N2}\boldsymbol{A}_2 \quad \cdots \quad b_{NN}\boldsymbol{A}_N) = \left(c_{N1}, \quad c_{N2}, \quad \cdots \quad c_{NN^2} \right) \end{cases}. \tag{3}$$

Now we introduce the third N-dimensional Walsh-Hadamard matrix $\boldsymbol{D}$, which consists of elements d_{jk} ($j = 1, 2, \ldots, N$ and $k = 1, 2, \ldots, N$) and be defined as:

$$\boldsymbol{D} = \begin{bmatrix} \boldsymbol{D}_1 \\ \boldsymbol{D}_2 \\ \vdots \\ \boldsymbol{D}_N \end{bmatrix} = \begin{bmatrix} d_{11} & d_{12} & \cdots & d_{1N} \\ d_{21} & d_{22} & \cdots & d_{2N} \\ \vdots & \vdots & \vdots & \vdots \\ d_{N1} & d_{N2} & \cdots & d_{NN} \end{bmatrix}. \tag{4}$$

Next, we utilize each $\boldsymbol{C}_i$ ($i = 1, 2, \ldots, N$) and $\boldsymbol{D}_j$ ($j = 1, 2, \ldots, N$) to generate a set of N sequences $\boldsymbol{E}_{ij}$ ($i, j = 1, 2, \ldots, N$) of length N^2 as:

$$\boldsymbol{E}_{ij} = \begin{pmatrix} c_{i1}d_{j1}, & c_{i2}d_{j2}, & \cdots, & c_{iN}d_{jN}, \\ c_{i(N+1)}d_{j1}, & c_{i(N+2)}d_{j2}, & \cdots, & c_{i(2N)}d_{jN}, \\ \vdots & \vdots & \vdots & \vdots \\ c_{i(N^2-N+1)}d_{j1}, & c_{i(N^2-N+2)}d_{j2}, & \cdots, & c_{i(N^2)}d_{jN} \end{pmatrix}. \tag{5}$$

Finally, the sequence sets $\{\boldsymbol{E}_{i1}, \boldsymbol{E}_{i2}, \ldots, \boldsymbol{E}_{iN}\}$ ($i = 1, 2, \ldots, N$) are used to constitute a set of complementary codes $\boldsymbol{Z}_i$ ($i = 1, 2, \ldots, N$) which can be written as:

$$\begin{cases} \boldsymbol{Z}_1 = \{\boldsymbol{Z}_{11}, \boldsymbol{Z}_{12}, \cdots, \boldsymbol{Z}_{1M}\} = \{\boldsymbol{E}_{11}, \boldsymbol{E}_{12}, \cdots, \boldsymbol{E}_{1N}\} \\ \boldsymbol{Z}_2 = \{\boldsymbol{Z}_{21}, \boldsymbol{Z}_{22}, \cdots, \boldsymbol{Z}_{2M}\} = \{\boldsymbol{E}_{21}, \boldsymbol{E}_{22}, \cdots, \boldsymbol{E}_{2N}\} \\ \vdots \quad \vdots \quad \vdots \\ \boldsymbol{Z}_N = \{\boldsymbol{Z}_{N1}, \boldsymbol{Z}_{N2}, \cdots, \boldsymbol{Z}_{NM}\} = \{\boldsymbol{E}_{N1}, \boldsymbol{E}_{N2}, \cdots, \boldsymbol{E}_{NN}\} \end{cases}, \tag{6}$$

Optics EXPRESS

where a set of CC codes contain N codes $\boldsymbol{Z}_i$ ($i = 1, 2, \ldots, N$), and each $\boldsymbol{Z}_i$ consists of M sub-codes $\boldsymbol{Z}_{ij}$ ($j = 1, 2, \ldots, M = N$) of length $L = N^2$. Therefore, we define CC code sets by three parameters, including code set size (N), sub-code number (M), and sub-code length (L), which can be denoted in a concise form as CC (N, M, L).

3.2. Example of CC code generation

Here, we take $N = 2$ for example. Let $\boldsymbol{A}$, $\boldsymbol{B}$ and $\boldsymbol{D}$ are the 2-dimensional Walsh-Hadamard matrices, which are described as:

$$\boldsymbol{A} = \boldsymbol{B} = \boldsymbol{D} = \begin{bmatrix} 1 & 1 \\ 1 & -1 \end{bmatrix} \tag{7}$$

Then, according to Eq. (3), matrices $\boldsymbol{C}$ can be obtained from

$$\begin{cases} \boldsymbol{C}_1 = \begin{pmatrix} 1 & 1 & 1 & -1 \end{pmatrix} \\ \boldsymbol{C}_2 = \begin{pmatrix} 1 & 1 & -1 & 1 \end{pmatrix} \end{cases}. \tag{8}$$

Next, we utilize each $\boldsymbol{C}_i$ ($i = 1, 2$) and $\boldsymbol{D}_j$ ($j = 1, 2$) to generate $\boldsymbol{E}_{ij}$ from:

$$\begin{cases} \boldsymbol{E}_{11} = \begin{pmatrix} 1 & 1 & 1 & -1 \end{pmatrix} \\ \boldsymbol{E}_{12} = \begin{pmatrix} 1 & -1 & 1 & 1 \end{pmatrix} \\ \boldsymbol{E}_{21} = \begin{pmatrix} 1 & 1 & -1 & 1 \end{pmatrix} \\ \boldsymbol{E}_{22} = \begin{pmatrix} 1 & -1 & -1 & -1 \end{pmatrix} \end{cases}. \tag{9}$$

Finally, the sequence sets $\boldsymbol{E}_{ij}$ are used to constitute a set of CC codes which can be written as:

$$\begin{aligned} \boldsymbol{Z}_1 &= \begin{cases} \boldsymbol{Z}_{11} = \boldsymbol{E}_{11} = \begin{pmatrix} 1 & 1 & 1 & -1 \end{pmatrix} \\ \boldsymbol{Z}_{12} = \boldsymbol{E}_{12} = \begin{pmatrix} 1 & -1 & 1 & 1 \end{pmatrix} \end{cases} \\ \boldsymbol{Z}_2 &= \begin{cases} \boldsymbol{Z}_{21} = \boldsymbol{E}_{21} = \begin{pmatrix} 1 & 1 & -1 & 1 \end{pmatrix} \\ \boldsymbol{Z}_{22} = \boldsymbol{E}_{22} = \begin{pmatrix} 1 & -1 & -1 & -1 \end{pmatrix} \end{cases} \end{aligned}, \tag{10}$$

where $\boldsymbol{Z}_1$ and $\boldsymbol{Z}_2$ are the two CC codes with parameters of (2, 2, 4).

3.3. Correlation properties of CC codes

Next, we delve into the correlation properties of CC codes, underscoring how their unique correlation characteristics allow them to maintain perfect orthogonality in asynchronous systems with continuous bitstream transmission. We will discuss the inherent properties of CC codes, notably their capability to uphold perfect periodic and aperiodic cross-correlation alongside auto-correlation, to emphasize their robustness and effectiveness in complex and non-synchronous environments.

First, the PCCFs between any pair of codes within the CC code set are zero for any possible relative chip shifts (τ), and the PACFs of each CC code are zero for all chip shifts except the zero shift [31]. Therefore, the periodic correlation function (PCF) of CC code can be described as the

Optics EXPRESS

following formula:

$$\rho(Z_i,\ Z_j;\ \tau) = \frac{1}{ML}\sum_{m=1}^{M}\sum_{n=0}^{L-1}\{Z_{im}(n)Z_{jm}[(n+\tau)\ \bmod\ L]\} = \begin{cases} 1, & i=j, \quad \tau=0 \\ 0, & i=j, \quad \tau\neq 0 \\ 0, & i\neq j, \quad \text{for any } \tau \end{cases}. \quad (11)$$

When $i=j$, Eq. (11) represents the PACFs of CC codes. When $i \neq j$, Eq. (11) becomes the PCCFs among CC codes. For simplicity in subsequent formulae, we define $<n+\tau>$ as $[(n+\tau)$ mod L]. Moreover, because CC codes have above-perfect periodic correlation properties, their aperiodic correlation function (ACF) also shows similar properties, which can be defined as:

$$\sigma(Z_i,\ Z_j;\ \tau) = \frac{1}{ML}\sum_{m=1}^{M}\sum_{n=0}^{L-1-\tau}\left[Z_{im}(n)Z_{jm}\left\langle n+\tau\right\rangle\right] = \begin{cases} 1, & i=j, \quad \tau=0 \\ 0, & i=j, \quad \tau\neq 0 \\ 0, & i\neq j, \ \text{for any } \tau \end{cases}. \quad (12)$$

When $i=j$, Eq. (12) represents the AACFs of CC codes. When $i \neq j$, Eq. (12) becomes the ACCFs among CC codes.

Due to the zero-valued PCCFs and ACCFs of CC codes, perfect orthogonality can be maintained among CC codes within the same group set during both synchronous and asynchronous transmissions. This orthogonality eliminates interference between VLCP signals encoded with CC codes, thus enabling MAI-free decoding. Concurrently, the PACFs and ACCFs of CC codes are zero under non-zero chip shifts. This implies that even in the presence of multipath propagation, the signals encoded by each CC code from all other paths except the desired one will be canceled out because of the auto-correlation properties of CC codes. As a result, accurate self-identification for the desired VLCP signal from each LED can be achieved, leading to an ISI-free transmission. Therefore, given the aforementioned advantageous correlation properties of CC codes, we design an integrated VLCP system based on MC-OCM by utilizing the perfect orthogonality of CC codes.

4. Asynchronous VLCP system based on MC-OCM and CC codes

4.1. System design and principle

Figure 2 illustrates the model and schematic diagram of the proposed indoor VLCP system based on MC-OCM. The system is equipped with four independently controlled LED transmitters mounted on the ceiling, serving as illumination sources and fulfilling the dual tasks of VLC and VLP. The system design takes into full consideration the complexity of the indoor environment, including the asynchrony in signal transmission, the multipath effects caused by line-of-sight (LOS) and non-line-of-sight (NLOS) paths, and the support for continuous bitstream transmission, all of which are common challenges in practical applications. The system's asynchronous transmission arises from different time delays associated with signals emitted by each LED, as well as the varying distances between the photodetectors (PD) and LEDs.

The signal processing begins with the encoding of user data. At the LED transmitters' end, we employ four independent encoders, each corresponding to one LED transmitter and equipped with a unique CC code for CDM, ensuring that multiple VLCP signals can be transmitted simultaneously without interference. The encoded data is then combined with a direct current (DC) bias and transmitted through the LED transmitter to emit VLCP signals. The photodetector (PD) at the receiver captures these VLCP signals and converts them back into electrical signals. Subsequently, decoders equipped with local copies of CC codes corresponding to specific LED transmitters in the signal processor perform correlation operations with the received signals.

Optics EXPRESS

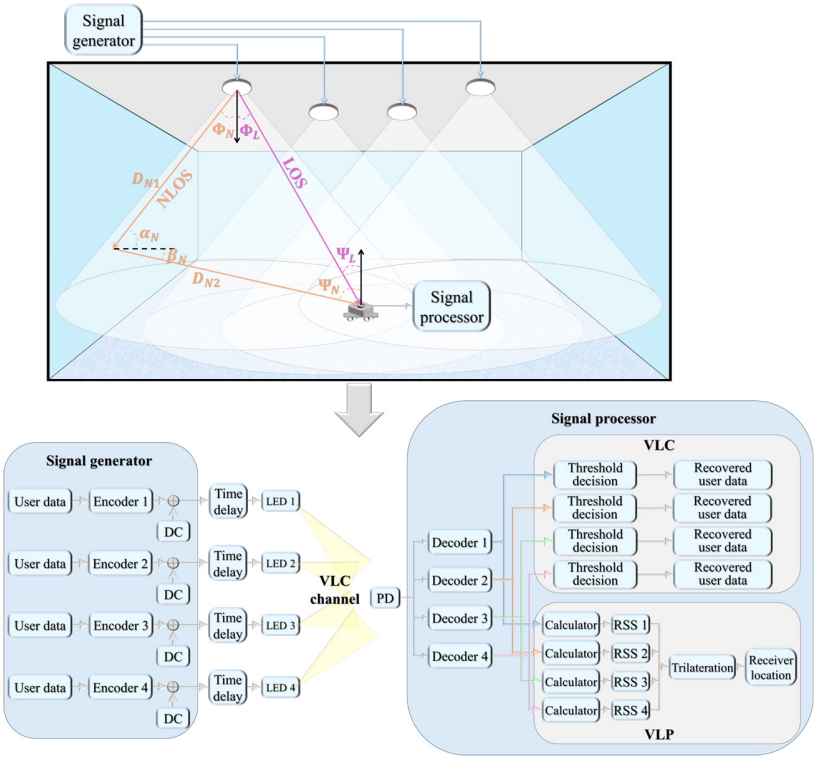

Fig. 2. System model and schematic diagram of the proposed indoor VLCP system based on MC-OCM.

Finally, we apply threshold judgment to the results of the correlation operations to recover user data for the VLC function. Simultaneously, we can derive RSS from the outcomes of the correlation operations and then combine it with trilateration algorithms to achieve the VLP function. A key innovation of the proposed VLCP system lies in the adoption of the MC-OCM strategy, allowing the transmission of multiple sub-codes of CC codes at the same time using orthogonal carriers. Figure 3 exemplifies this process, demonstrating the encoding and decoding mechanisms of MC-OCM with a four-sub-code CC code set. Here, we assign CC code $\mathbf{Z}_i$ to the i-th encoder and decoder, which is tasked with processing the VLCP signal from the i-th LED. Below, we detail the foundational principles underlying this implementation.

Firstly, the user data is sent to the encoder for encoding. As shown in Fig. 3, the user data for the i-th LED is encoded by sub-codes $\mathbf{Z}_{ij}$ ($j = 1, 2, \ldots, M$) of the i-th CC code $\mathbf{Z}_i$, respectively. The k-th symbol of user data encoded by $\mathbf{Z}_{ij}$ is described as:

$$e_{ijk}(t) = u_{ik}\mathbf{Z}_{ij}(t),\ (k-1)L \le t < kL, \tag{13}$$

where $u_{ik} \in \{-1, 1\}$ is the k-th symbol of user data for the i-th LED. Subsequently, each encoded sub-data e_{ij} ($j = 1, 2, \ldots, M$) is individually modulated by one of four orthogonal carriers, each with a frequency f_j ($j = 1, 2, \ldots, M$), respectively. The modulated data for the k-th symbol of the j-th sub-data for the i-th LED can be formulated as:

$$s_{ijk}(t) = e_{ijk}(t)\cos(2\pi f_j t + \theta_i),\ (k-1)T_c L \le t < kT_c L, \tag{14}$$

where θ_i is the initial phase of the signal for the i-th LED, and T_c is one chip duration of sub-code $\mathbf{Z}_{ij}$, which is equal to the integer multiple of the carrier period. Thus, the duration of the k-th

Optics EXPRESS

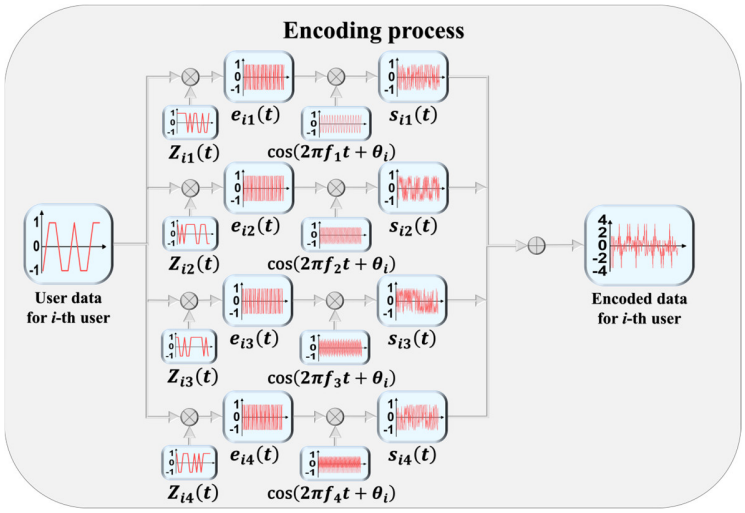

Fig. 3. Schematic diagram of MC-OCM scheme for the encoding process. The waveforms in the blue box illustrate the waveform diagram of the signal sent to the i-th LED and the signal received at the (0, 0) point.

symbol is equal to T_c L. After summing all the modulated sub-data s_{ij} ($j = 1, 2, \ldots, M$), we can obtain the encoded user data sent to the i-th LED, which can be written as:

$$S_i(t) = \sum_{j=1}^{M} s_{ij}(t). \tag{15}$$

Next, adding the DC component and random time delay to the encoded data generated by the i-th encoder, the i-th VLCP signal (i.e., the signal transmitting from the i-th LED) can be given as:

$$T_i(t) = P_t(\delta S_i(t + \Delta t_{\mathrm{LED}i}) + 1), \tag{16}$$

where P_t is the optical power of each LED, $\Delta t_{\mathrm{LED}i}$ represents the relative time delay of the i-th VLCP signal, and δ is the modulation index which refers to the ratio between the maximum current variation caused by the alternating current signal and the direct current signal [33].

After passing through the VLC channel, the VLCP signals from all LEDs are received by the PD and converted into an electrical signal. Then, the received VLCP signal can be represented as:

$$R(t) = \gamma \sum_{i=1}^{N} [T_i(t) * H_{i\mathrm{LOS}}(t) + T_i(t) * H_{i\mathrm{NLOS}}(t)] + N_{\mathrm{AWGN}}(t), \tag{17}$$

where * means convolution operation, γ is the PD responsivity, $H_{i\mathrm{LOS}}$ and $H_{i\mathrm{NLOS}}$ represent the impulse responses of LOS and NLOS channels for the i-th VLCP signal, respectively, and N_{AWGN} stands for the additive white Gaussian noise (AWGN). In this paper, $T_i(t)_* H_{i\mathrm{LOS}}(t)$ constitutes the desired signal, whereas $T_i(t)_* H_{i\mathrm{NLOS}}(t)$ is the interference signal induced by multipath propagation. To streamline the analysis, we only consider the first reflection of the wall. Thus, the DC gains of LOS and NLOS channels can be expressed as [34]:

$$\begin{cases} h_{\mathrm{LOS}} = \frac{(ml+1)A_{\mathrm{r}}}{2\pi D_{\mathrm{L}}^2} \cos^{ml}(\Phi_{\mathrm{L}}) T_{\mathrm{s}}(\Psi_{\mathrm{L}}) g_{\mathrm{c}}(\Psi_{\mathrm{L}}) \cos(\Psi_{\mathrm{L}}) \\ \mathrm{d}h_{\mathrm{NLOS}} = \frac{(ml+1)A_{\mathrm{r}}\rho_{\mathrm{r}}\mathrm{d}A_{\mathrm{wall}}}{2\pi^2 D_{\mathrm{N1}}^2 D_{\mathrm{N2}}^2} \cos^{ml}(\Phi_{\mathrm{N}}) \cos(\alpha_{\mathrm{N}}) \cos(\beta_{\mathrm{N}}) T_{\mathrm{s}}(\Psi_{\mathrm{N}}) g_{\mathrm{c}}(\Psi_{\mathrm{N}}) \cos(\Psi_{\mathrm{N}}) \end{cases}, \tag{18}$$

Optics EXPRESS

where ml is Lambertian order, A_{r} is the effective receiving area of PD, T_{s} is the optical filter's gain, g_{c} is the optical concentrator's gain, ρ_{r} is the reflectance factor, and $\mathrm{d}A_{\mathrm{wall}}$ indicates the reflective area of a small region. The LOS channel is characterized by Φ_{L}, Ψ_{L}, and D_{L}, which correspond to the angle of incidence, the angle of irradiance, and the transmission distance, respectively. Conversely, for the NLOS channel, Φ_{N}, Ψ_{N}, α_{N}, β_{N}, and $D_{\mathrm{N1}} + D_{\mathrm{N2}}$ represent the angle of incidence, the angle of irradiance, the angle of irradiance to a reflective point, the angle of irradiance to the receiver, and the total transmission distance, respectively. Then the noise variance of N_{AWGN} is given by:

$$\begin{aligned}
&\sigma_{\mathrm{A}}^2 = \sigma_{\mathrm{s}}^2 + \sigma_{\mathrm{t}}^2 \\
&\text{where} \begin{cases} \sigma_{\mathrm{s}}^2 = 2q\left[\gamma P_t\left(h_{\mathrm{LOS}} + \int_{\mathrm{walls}} dh_{\mathrm{NLOS}}\right) + I_{bg} I_2\right] B_n \\ \sigma_{\mathrm{t}}^2 = 8\pi k T_k \eta A_r B_n^2 (I_2/G + 2\pi\Gamma\eta A_r I_3 B_n/g_m) \end{cases} .
\end{aligned} \tag{19}$$

In Eq. (19), ${\sigma_{\mathrm{s}}}^2$ and ${\sigma_{\mathrm{t}}}^2$ denote the variances of shot noise and thermal noise, respectively. Here, q stands for the electronic charge, I_{bg} denotes the background current, I_2 refers to noise bandwidth factor, B_{n} represents the equivalent noise bandwidth, equal to the system modulation bandwidth, k is the Boltzmann constant, T_k is absolute temperature, η is fixed capacitance of PD per unit area, G is open loop voltage gain, Γ is FET channel noise factor, I_3 is gate-induced drain leakage, and g_m is FET transconductance. The numerical values of these parameters will be provided in the simulation setup.

Then, the received data is forwarded to the decoder for decoding. The decoding process is outlined in Fig. 4. First, the received data undergoes demodulation by carriers of frequency f_j ($j = 1, 2, \ldots, M$), yielding the demodulated sub-data. Under the assumption of ideal carrier-phase coherence, the z-th chip of the k-th symbol within the j-th demodulated sub-data for the i-th VLCP signal can be mathematically described as:

$$\begin{aligned}
&ds_{ijk}(z) = \sum_{n=T_c(z-1)}^{zT_c-1} R(n) \times 2\cos(2\pi f_j n + \theta_i) \\
&= \gamma P_t \delta \sum_{i=1}^{N} \left[h_{\mathrm{LOS}i} u_{ia} \boldsymbol{Z}_{ij} \langle z + \tau_{\mathrm{LOS}i}\rangle + \int_{\mathrm{walls}} dh_{\mathrm{NLOS}i} u_{ib} \boldsymbol{Z}_{ij} \langle z + \tau_{\mathrm{NLOS}i}\rangle\right](1 + \varpi_l) + N_{nsij}(z), \\
&\text{where } \varpi_l = \cos(\theta_l - \theta_i),\ N_{nsij}(z) = \sum_{n=T_c(z-1)}^{zT_c-1} N_{\mathrm{AWGN}}(n) \times 2\cos(2\pi f_j n + \theta_i), \\
&\begin{cases} a = (k-1), & (k-1)L \le z < (k-1)L + \tau_{\mathrm{LOS}i} \\ a = k, & (k-1)L + \tau_{\mathrm{LOS}i} \le z < kL \end{cases}, \\
&\text{and} \begin{cases} b = (k-1), & (k-1)L \le z < (k-1)L + \tau_{\mathrm{NLOS}i} \\ b = k, & (k-1)L + \tau_{\mathrm{NLOS}i} \le z < kL \end{cases}.
\end{aligned} \tag{20}$$

In Eq. (20), $\tau_{\mathrm{LOS}i}$ and $\tau_{\mathrm{NLOS}i}$ are the relative chip shifts caused by the time delay experienced by i-th VLCP signal traversing LOS and NLOS channels, respectively. For simplification, it is presumed that all the NLOS channels affecting the i-th VLCP signal induce the same chip shifts. Both $\tau_{\mathrm{LOS}i}$ and $\tau_{\mathrm{NLOS}i}$ are integer multiples of the CC code chip duration and are bounded within one period of $\boldsymbol{Z}_{ij}$, i.e., $\tau_{\mathrm{LOS}i}, \tau_{\mathrm{NLOS}i} = 0, 1, \ldots, T_c L$. The proof process of Eq. (20) is provided in Appendix A.

Afterward, the local correlator consisting of reference code $\boldsymbol{Z}_{ij}$ ($j = 1, 2, \ldots, M$) is used to decode the demodulated sub-data of the i-th VLCP signal. To simplify the expression, we assume that when decoding the i-th VLCP signal, the initial position of the signal can consistently be pinpointed. This can be facilitated by appending a pilot sequence to each signal frame.

Optics EXPRESS

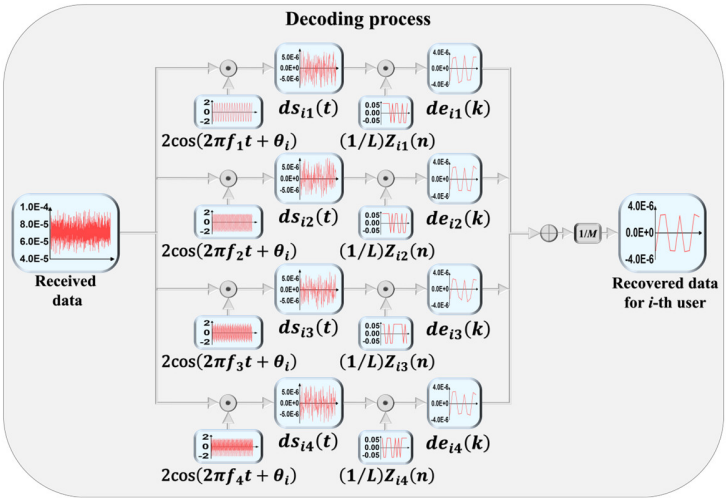

Fig. 4. Schematic diagram of MC-OCM scheme for the decoding process. The waveforms in the blue box illustrate the waveform diagram of the signal sent to the i-th LED and the signal received at the (0, 0) point.

Consequently, the decoded k-th symbol of the j-th sub-data for the i-th VLCP signal can be represented as follows:

$$
\begin{aligned}
de_{ijk} &= \sum_{n=0}^{L-1} ds_{ijk}(n) \times \tfrac{1}{L}\mathbf{Z}_{ij}(n) \\
&= \gamma P_t \delta \tfrac{1}{L} \Bigg\{ h_{\mathrm{LOS}i} \sum_{n=0}^{L-1} u_k \mathbf{Z}_{ij}(n)\mathbf{Z}_{ij}(n) \\
&+ \int_{\mathrm{walls}} dh_{\mathrm{NLOS}i} \left[\sum_{n=0}^{\tilde{\tau}_{\mathrm{NLOS}i}-1} u_{i(k-1)} \mathbf{Z}_{ij}\left\langle n + \tilde{\tau}_{\mathrm{NLOS}i} \right\rangle \mathbf{Z}_{ij}(n) + \sum_{n=\tilde{\tau}_{\mathrm{NLOS}i}}^{L-1} u_{ik} \mathbf{Z}_{ij}\left\langle n + \tilde{\tau}_{\mathrm{NLOS}i} \right\rangle \mathbf{Z}_{ij}(n) \right] \\
&+ \sum_{\substack{l=1, \\ l\neq i}}^{N} h_{\mathrm{LOS}l} \left[\sum_{n=0}^{\tilde{\tau}_{\mathrm{LOS}l}-1} u_{l(k-1)} \mathbf{Z}_{lj}\left\langle n + \tilde{\tau}_{\mathrm{LOS}l} \right\rangle \mathbf{Z}_{ij}(n) + \sum_{n=\tilde{\tau}_{\mathrm{LOS}l}}^{L-1} u_{lk} \mathbf{Z}_{lj}\left\langle n + \tilde{\tau}_{\mathrm{LOS}l} \right\rangle \mathbf{Z}_{ij}(n) \right] (1+\varpi_l) \\
&+ \sum_{\substack{l=1, \\ l\neq i}}^{N} \int_{\mathrm{walls}} dh_{\mathrm{NLOS}l} \left[\begin{array}{l} \sum_{n=0}^{\tilde{\tau}_{\mathrm{NLOS}l}-1} u_{l(k-1)} \mathbf{Z}_{lj}\left\langle n + \tilde{\tau}_{\mathrm{NLOS}l} \right\rangle \mathbf{Z}_{ij}(n) + \\ \sum_{n=\tilde{\tau}_{\mathrm{NLOS}l}}^{L-1} u_{lk} \mathbf{Z}_{lj}\left\langle n + \tilde{\tau}_{\mathrm{NLOS}l} \right\rangle \mathbf{Z}_{ij}(n) \end{array} \right] (1+\varpi_l) \Bigg\} \\
&+ \tfrac{1}{L} \sum_{n=0}^{L-1} N_{nsij}(t) \times \mathbf{Z}_{ij}(n),
\end{aligned}
$$

where $\tilde{\tau}_{\mathrm{NLOS}i} = \tau_{\mathrm{NLOS}i} - \tau_{\mathrm{LOS}i}$, $\tilde{\tau}_{\mathrm{LOS}l} = \tau_{\mathrm{LOS}l} - \tau_{\mathrm{LOS}i}$, and $\tilde{\tau}_{\mathrm{NLOS}l} = \tau_{\mathrm{NLOS}l} - \tau_{\mathrm{LOS}i}$.

(21)

Optics EXPRESS

Finally, by summing all the demodulated sub-data from Eq. (21), we can obtain the correlation value between the k-th symbol of the i-th VLCP signal and the local reference codeword from:

$$\begin{aligned}
&\Im_{ik} = \tfrac{1}{M}\sum_{j=1}^{M} de_{ijk} \\
&= \gamma P_t \delta h_{\mathrm{LOS}i} u_k \rho(\mathbf{Z}_i,\ \mathbf{Z}_i;\ 0) + ISI + MAI + AWGN \\
&\text{where } ISI = \gamma P_t \delta \int_{\mathrm{walls}} dh_{\mathrm{NLOS}i}[u_{i(k-1)}\sigma(\mathbf{Z}_i,\ \mathbf{Z}_i;\ \tilde{\tau}_{\mathrm{NLOS}i}) + u_{ik}\sigma(\mathbf{Z}_i,\ \mathbf{Z}_i;\ L-\tilde{\tau}_{\mathrm{NLOS}i})], \\
&MAI = \gamma P_t \delta \left\{ \begin{array}{l} \sum\limits_{\substack{l=1,\\ l\neq i}}^{N} h_{\mathrm{LOS}l}[u_{l(k-1)}\sigma(\mathbf{Z}_i,\ \mathbf{Z}_l;\tilde{\tau}_{\mathrm{LOS}l}) + u_{lk}\sigma(\mathbf{Z}_i,\ \mathbf{Z}_l;L-\tilde{\tau}_{\mathrm{LOS}l})](1+\varpi_l) \\ + \sum\limits_{\substack{l=1,\\ l\neq i}}^{N} \int_{\mathrm{walls}} dh_{\mathrm{NLOS}l} \left[\begin{array}{l} u_{l(k-1)}\sigma(\mathbf{Z}_i,\ \mathbf{Z}_l;\ \tilde{\tau}_{\mathrm{NLOS}l}) + \\ u_{lk}\sigma(\mathbf{Z}_i,\ \mathbf{Z}_l;L-\tilde{\tau}_{\mathrm{NLOS}l}) \end{array} \right](1+\varpi_l) \end{array} \right\}, \\
&\text{and } AWGN = \tfrac{1}{ML}\sum_{j=1}^{M}\sum_{n=0}^{L-1} N_{nsij}(n) \times \mathbf{Z}_{ij}(n).
\end{aligned} \tag{22}$$

The proof process of Eq. (22) is provided in Appendix B. In Eq. (22), *ISI* means the ISI caused by the NLOS channels, *MAI* is the MAI caused by the VLPC signals from other LEDs, and *AWGN* is the AWGN reduced by processing gain of CC codes [32].

Then, according to the PCFs and ACFs of CC codes shown in Eq. (11) and Eq. (12), we can obtain the results as follows:

$$\left\{ \begin{array}{l} \rho(\mathbf{Z}_i,\ \mathbf{Z}_i;\ 0) = 1 \\ \sigma(\mathbf{Z}_i,\ \mathbf{Z}_i;\ \tilde{\tau}_{\mathrm{NLOS}i}) = \sigma(\mathbf{Z}_i,\ \mathbf{Z}_i;\ L-\tilde{\tau}_{\mathrm{NLOS}i}) = 0 \\ \sigma(\mathbf{Z}_i,\ \mathbf{Z}_l;\tilde{\tau}_{\mathrm{LOS}l}) = \sigma(\mathbf{Z}_i,\ \mathbf{Z}_l;L-\tilde{\tau}_{\mathrm{LOS}l}) = 0 \\ \sigma(\mathbf{Z}_i,\ \mathbf{Z}_l;\ \tilde{\tau}_{\mathrm{NLOS}l}) = \sigma(\mathbf{Z}_i,\ \mathbf{Z}_l;L-\tilde{\tau}_{\mathrm{NLOS}l}) = 0 \end{array} \right. . \tag{23}$$

Therefore, in Eq. (22), both *MAI* and *ISI* can be effectively reduced to zero. This theoretically validates that the proposed MC-OCM scheme based on CC codes can fundamentally mitigate the impact of MAI and ISI on demodulating VLCP signals. Then, the Eq. (22) can be rewritten as:

$$\Im_{ik} = \gamma P_t \delta h_{\mathrm{LOS}i} u_{ik} + AWGN. \tag{24}$$

Then, to realize the VLC function, we recover user data by thresholding the correlation values obtained from Eq. (24), as shown in the following equation:

$$\tilde{u}_{ik} = \left\{ \begin{array}{ll} 1, & \Im_{ik}>0 \\ -1, & \Im_{ik}<0 \end{array} \right. . \tag{25}$$

In the meantime, as for realizing the VLP function, firstly, the RSS of the i-th VLCP signal is obtained by using the calculator from:

$$\Re_{ik} = |\Im_{ik}| = \gamma P_t \delta h_{\mathrm{LOS}i} + N_{noise}, \tag{26}$$

where N_{noise} is the interference caused by AWGN. To simplify the system, we assume that the receiving surface of the PD is parallel to the emitting surface of the LED. Then, by substituting Eq. (18) into Eq. (26) and performing simple transformations, we can obtain the transmission

Optics EXPRESS

distance of the i-th VLCP signal from:

$$\tilde{D}_{ik} = \left[\frac{(ml+1)A_r h^{m_l+1}}{2\pi} T_s(\Psi_L) g_c(\Psi_L) \gamma P_t \delta\right]^{[1/(m_l+3)]} (\Re_{ik} - N_{noise})^{-[1/(m_l+3)]}, \tag{27}$$

where h is the vertical distance between LED and PD. Due to the longer transmission distance, the signal strength becomes weaker, making it more susceptible to noise and interference. Thus, to mitigate the impact of poor signals on positioning, we eliminate the VLCP signal with the maximum transmission distance, retaining the remaining three VLCP signals for trilateration to determine the PD's position which can be calculated from:

$$\begin{bmatrix} X_2 - X_1 & Y_2 - Y_1 \\ X_3 - X_1 & Y_3 - Y_1 \end{bmatrix} \begin{bmatrix} \tilde{x} \\ \tilde{y} \end{bmatrix} = \frac{1}{2} \begin{bmatrix} X_2^2 + Y_2^2 - (X_1^2 + Y_1^2) + \tilde{D}_{1,k}^2 - \tilde{D}_{2k}^2 \\ X_3^2 + Y_3^2 - (X_1^2 + Y_1^2) + \tilde{D}_{1,k}^2 - \tilde{D}_{3k}^2 \end{bmatrix}, \tag{28}$$

where (X_i, Y_i) are the coordinates of corresponding LEDs with selected VLCP signals and $(\tilde{x}, \tilde{y})$ is the estimated location of PD. Since the measurement error of the signal transmission distance poses challenges to solving the aforementioned formula, we resort to employing the least squares estimation (LSE) method to solve Eq. (28).

4.2. Simulation setup

Due to equipment and space constraints, we focus on simulations to validate the proposed scheme in this paper. As illustrated in Fig. 2, the VLCP system is simulated in a room model with a size of 5 m × 5 m × 3 m. Four LED transmitters are evenly distributed on the ceiling and oriented towards the floor, while a PD receiver is placed on the floor and oriented towards the ceiling. Their transmitting and receiving planes are kept parallel with a vertical distance of 2.15 meters. The X-Y coordinates of these transmitters are denoted as LED_1 (−1.25 m, 1.25 m), LED_2 (1.25 m, 1.25 m), LED_3 (−1.25 m, −1.25 m), and LED_4 (1.25 m, −1.25 m), respectively. Across a 4 m × 4 m receiving plane, 41 × 41 test points are uniformly arranged, and the PD traverses these positions sequentially to capture VLCP signals from the four LEDs.

To facilitate the VLCP system based on MC-OCM, we assign a set of CC codes with parameters of (4, 4, 16) to these four LEDs for CDM. Additionally, for comprehensive performance evaluation and comparison with existing technologies, we include two other encoding schemes: one described as CDM based on ZCZ codes in [20], and the other mentioned as CDM based on COWH codes in [30]. To ensure experimental consistency, the lengths of all codewords are set to 16. The bit error rate (BER) and positioning error (PE) at each test point for VLCP systems utilizing these three coding approaches are estimated. Among them, PE is defined as the Euclidean distance between the estimated position and the actual position of the PD, which can be described as:

$$PE = \sqrt{(x - \tilde{x})^2 + (y - \tilde{y})^2}, \tag{29}$$

where (x, y) and $(\tilde{x}, \tilde{y})$ are the real and estimated location of PD, respectively. We perform these tests across four different scenarios. Specifically, the simulations are conducted under the following four scenarios: S.i. synchronous system without considering NLOS channels (syn. w/o NLOS), S.ii. asynchronous system without considering NLOS channels (asyn. w/o NLOS), S.iii. synchronous system considering NLOS channels (syn. w/ NLOS), and S.iv. asynchronous system considering NLOS channels (asyn. w/ NLOS). The other simulation parameters and their values are given in Table 1.

Optics EXPRESS

Table 1. Simulation parameters

Parameters	Symbol	Value
The output power of each LED	P_t	10 W
Modulation index	δ	0.15
Photodetector responsivity	γ	0.4
Lambertian order	ml	1
The effective receiving area of PD	A_{r}	75.4 mm^2
Gain of an optical filter	T_{s}	1
Gain of an optical concentrator	g_{c}	2.4115
Reflectance factor	ρ_{r}	0.7
Reflective area of a small region	$\mathrm{d}A_{\mathrm{wall}}$	1 cm^2
Electronic charge	q	1.6×10^{-19} C
Background current	I_{bg}	5100 uA
Noise bandwidth factor	I_2	0.562
Equivalent noise bandwidth	B_{n}	10 GHz
Denotes Boltzmann's constant	k	$1.38064852 \times 10^{-23}$ m^2 kg s^{-2} K^{-1}
Absolute temperature	T_k	295 K
Fixed capacitance of photodetector per unit area	η	112 $\mathrm{pF/cm}^2$
Open loop voltage gain	G	10
FET channel noise factor	Γ	1.5
Gate-induced drain leakage	I_3	0.0868
FET transconductance	g_m	30 mS
The initial phase of the signal	θ_i	30°, 60°, 90°, 120°
The volume of measured data for each LED		1×10^5 bits

5. Results and discussions

First, we individually validate the correlation properties of the employed CC codes, ZCZ codes, and COWH codes, each with a code length of 16. The PCF and ACF properties of these three code types are shown in Fig. 5. Regarding CC codes, both their PACFs and AACFs are zero under non-zero chip offsets, and meanwhile, their PCCFs and ACCFs are zero for any chip offset. This demonstrates that CC codes maintain perfect cross-correlation and auto-correlation properties in both synchronous and asynchronous systems. For ZCZ codes, they exhibit zero-valued PCCFs within the zero-correlation zone, i.e., chip offset ≤ 1, accompanied by PACFs featuring low sidelobes and a singular peak. Conversely, COWH codes present zero-valued PCCFs across all chip offsets, but their PACFs display high sidelobes and multiple peaks. Additionally, both ZCZ and COWH codes have complex AACFs and ACCFs. As a result, while ZCZ codes and COWH codes can preserve favorable cross-correlation and auto-correlation properties in synchronized systems, their performance deteriorates in asynchronous systems with continuous bitstream transmission.

Then, we evaluate the performance of VLCP systems based on CC codes, ZCZ codes, and COWH codes in syn. w/o NLOS systems, as depicted by the surface distributions of BER and PE in Fig. 6. The results reveal similar spatial distribution trends of BER and PE among the three encoding schemes: BER and PE values are minimized in the room's central area, increasing as the receiver approaches the room boundaries. This phenomenon stems from the influence of receiver position on total received optical intensity, with the central position typically experiencing higher intensity, resulting in higher signal-to-noise ratios (SNR) compared to edge regions. Remarkably,

Optics EXPRESS

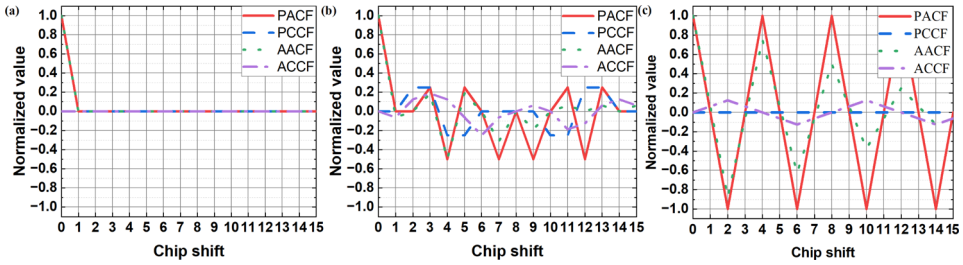

Fig. 5. The normalized PCF and ACF values of (a) CC codes; (b) ZCZ codes; and (c) COWH codes varying different chip shifts.

even under such ideal synchronous conditions, the CC codes outperform the ZCZ and COWH codes in terms of BER and PE. This superiority arises from the inherent coding gain of CC codes, directly related to the product of the number and length of sub-codes [32]. Therefore, even with the same code length, CC codes, leveraging their multi-sub-code structure, achieve higher coding gains than ZCZ codes and COWH codes, more effectively combating AWGN and achieving superior communication and positioning performance. Further analysis of the cumulative distribution function (CDF) curves for BER and PE calculated from all test points, as shown in Fig. 7, demonstrates that 90% of test points in VLCP systems based on CC codes exhibit BER below the forward error correction (FEC) standard of 3.8E−3. In contrast, this proportion is only 67% for systems based on ZCZ and COWH codes, highlighting the significant advantage of CC codes in ensuring communication quality. Similarly, in terms of positioning accuracy, approximately 99% of test points in CC codes-based VLCP systems have PE below 10 cm, whereas only about 75% of test points achieve the same positioning accuracy with ZCZ and COWH codes, emphasizing once again the outstanding performance of CC codes in improving positioning accuracy. Additionally, the reason ZCZ and COWH exhibit the same performance in Fig. 7 is that they both can maintain orthogonality in the synchronous system and have the same code length and gain. Overall, CC codes demonstrate significant advantages over ZCZ codes and COWH codes in reducing the impact of AWGN.

Next, we conduct extensive tests on three encoding schemes in asyn. w/o NLOS VLCP system, aiming to validate their ability to resist MAI caused by asynchronous transmission. The experimental results, depicted in Fig. 8, clearly demonstrate the differences in performance in terms of BER and PE among the different coding schemes. Particularly noteworthy is the consistently high performance of MC-OCM based on CC codes in both communication reliability and positioning accuracy, indicating their effective suppression of interference introduced by various VLCP signals from different LED transmitters. This is attributed to the excellent PCCF and ACCF of CC codes, ensuring high orthogonality between VLCP signals in asynchronous systems, thereby achieving low BER and PE. In contrast, ZCZ and COWH codes exhibit notable degradation in performance within asynchronous systems, as manifested by sharply increased BER and PE values. This performance decline is attributed to compromised orthogonality, leading to exacerbated interference between VLCP signals from different LED transmitters. Among these, COWH codes slightly outperform ZCZ codes, benefiting from their better PCCF properties, where the PCCF of COWH is zero for all chip offsets, while ZCZ achieves this effect only in specific zero-correlation zones. Moreover, the CDF curves (Fig. 9) of BER and PE further corroborate these findings: VLCP systems based on CC codes achieve BER below the FEC threshold in over 90% of test points, demonstrating good communication stability. In contrast, VLCP systems based on ZCZ and COWH codes only meet this standard in approximately 8% and 17% of test points, respectively. Regarding positioning accuracy, the superiority of CC codes is more pronounced, with approximately 99% of test points recording PE below 10 cm,

Optics EXPRESS

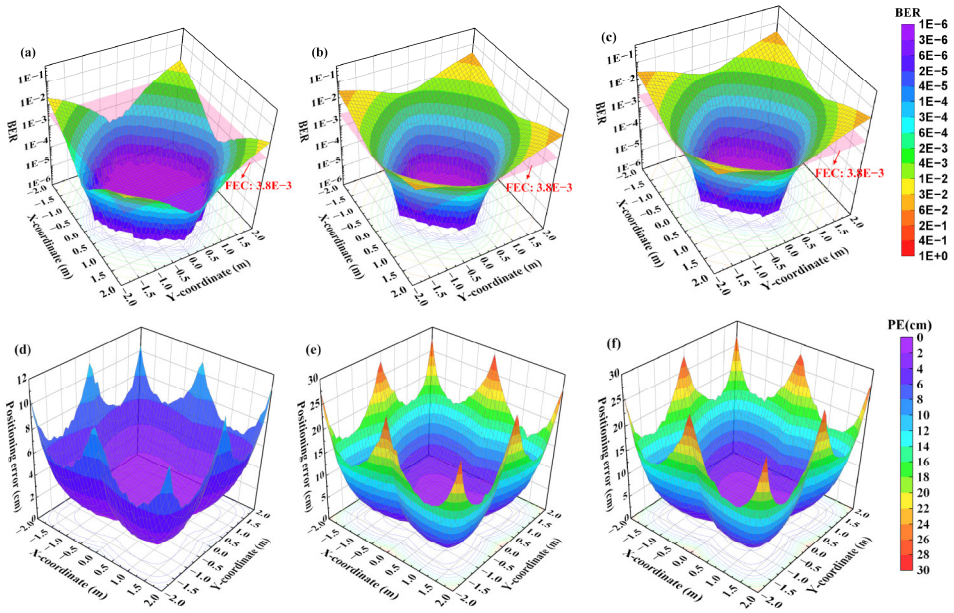

Fig. 6. For syn. w/o NLOS VLCP systems: Color-mapped surface plots of the BER based on (a) CC codes; (b) ZCZ codes; and (c) COWH codes, where the pink planes represent the FEC criterion of 3.8E−3. Surface plots of the PE based on (d) CC codes; (e) ZCZ codes; and (f) COWH codes.

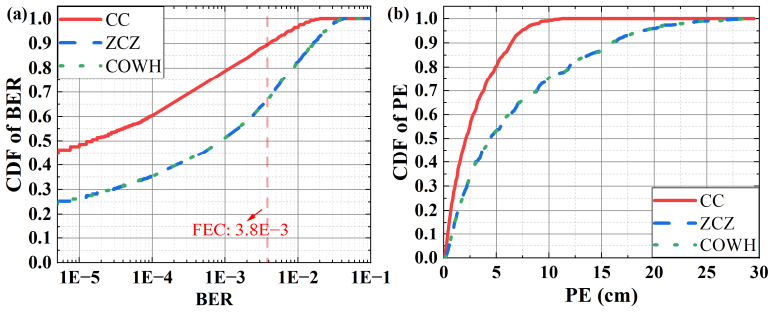

Fig. 7. For syn. w/o NLOS VLCP systems: CDF curve of the (a) BER; and (b) PE, based on different codes, where the pink line in (a) represents the FEC criterion of 3.8E−3.

Optics EXPRESS

far exceeding 7% for ZCZ codes and 13% for COWH codes. These data strongly demonstrate the significant superiority and robustness of CC codes against the MAI in asynchronous VLCP systems.

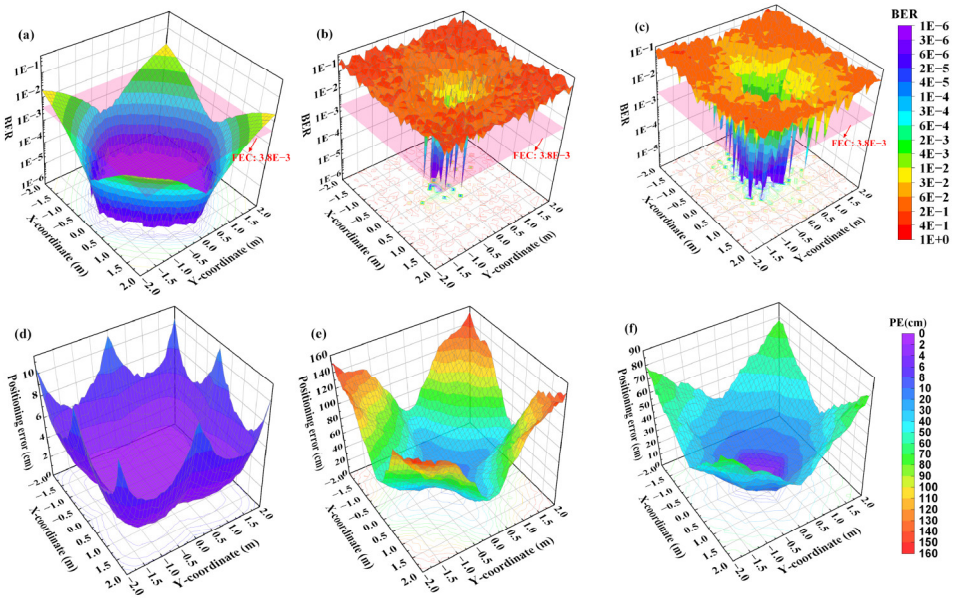

Fig. 8. For asyn. w/o NLOS VLCP systems: Color-mapped surface plots of the BER based on (a) CC codes; (b) ZCZ codes; and (c) COWH codes, where the pink planes represent the FEC criterion of 3.8E−3. Surface plots of the PE based on (d) CC codes; (e) ZCZ codes; and (f) COWH codes.

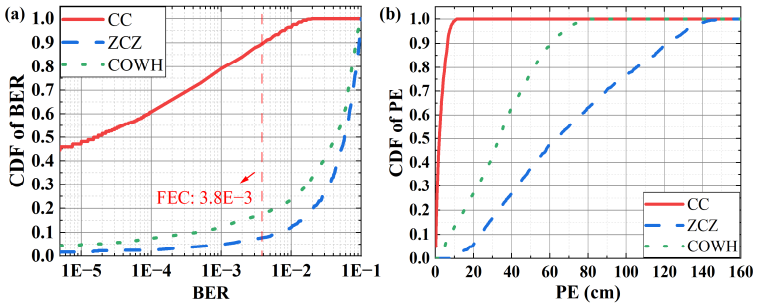

Fig. 9. For asyn. w/o NLOS VLCP systems: CDF curve of the (a) BER; and (b) PE, based on different codes, where the pink line in (a) represents the FEC criterion of 3.8E−3.

Subsequently, we conduct a comparison of the performance of these three coding strategies in syn. w/o NLOS VLCP systems to assess their ability to combat multipath-induced ISI. Figure 10 illustrates color-mapped surface plots of estimated BER and PE in this scenario. In regions near the room edges, the PE for all three encoding schemes significantly increases. This is attributed not only to SNR attenuation but also to the near-simultaneous detection of direct and wall-reflected light by the receiver. Because the optical path difference between direct light and wall-reflected light in these areas is very small, often with the time difference being less than the duration of a single code chip, it is impossible to distinguish between direct and reflected signals at the chip level. This leads to deviations in the correlation values calculated according to

Optics EXPRESS

Eq. (24). Given that the RSS employed for VLP, as stipulated by Eq. (26), is directly derived from these correlation values, such deviation directly affects positioning precision. Despite contending with multipath effects, CC codes demonstrate significant advantages over ZCZ codes and COWH codes in terms of both BER and PE, as shown in Fig. 11. CC codes maintain a BER below the FEC threshold at approximately 90% of measurement points, with PE below 6.65 cm. In terms of communication performance, ZCZ codes and COWH codes perform similarly, with approximately 64% of measurement points meeting the FEC requirements. This is because the thresholding method is used to recover data, which is more tolerant of CV errors. Thus, ISI has a relatively small effect on the communication quality of both ZCZ and COWH, resulting in similar BER performance. Regarding positioning performance, ZCZ codes slightly outperform COWH codes, with approximately 53% and 48% of measurement points attaining PE below 6.65 centimeters, respectively. This advantage stems from the lower secondary lobes of the PACF and AACF of ZCZ codes compared to COWH codes, facilitating more effective mitigation of multipath effects and reducing the adverse effects of ISI. In summary, CC codes exhibit the best robustness in resisting ISI and maintaining communication and positioning performance, while ZCZ codes demonstrate better positioning performance compared to COWH codes in syn. w/o NLOS VLCP systems.

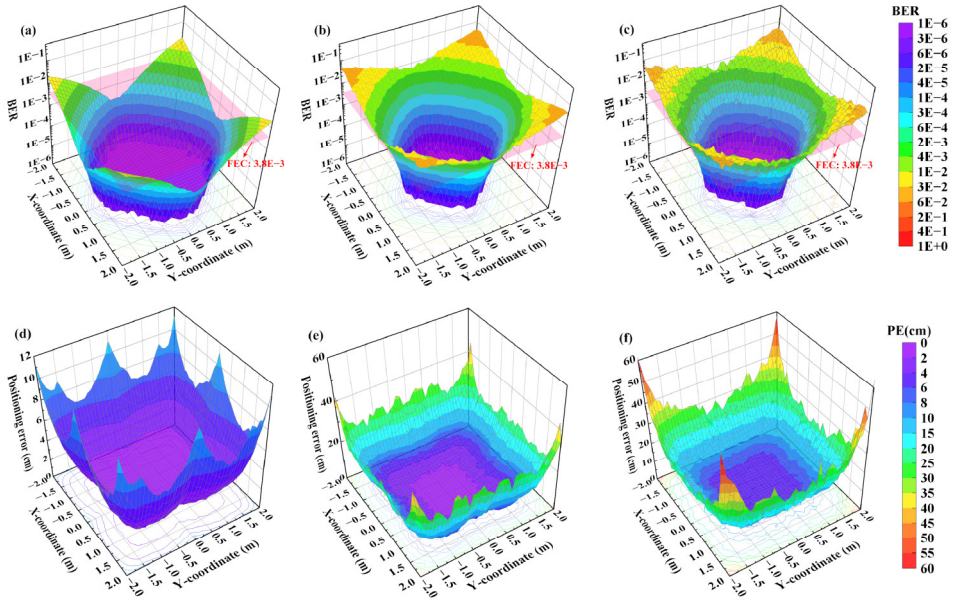

Fig. 10. For syn. w/ NLOS VLCP systems: Color-mapped surface plots of the BER based on (a) CC codes; (b) ZCZ codes; and (c) COWH codes, where the pink planes represent the FEC criterion of 3.8E−3. Surface plots of the PE based on (d) CC codes; (e) ZCZ codes; and (f) COWH codes.

Furthermore, we evaluate the comprehensive performance of the three encoding schemes in asyn. w/ NLOS VLCP systems. The simulation results, summarized in Fig. 12 and Fig. 13, clearly demonstrate the adaptability of each coding scheme under asynchronous transmission and multipath propagation. As expected, the CC codes continue to demonstrate their superiority, with approximately 90% of measurement points maintaining a BER below the FEC error correction threshold, while an impressive 99% of measurement points achieve high-precision positioning with errors below 10 cm. Following this, the COWH codes achieve FEC-standard BER in approximately 17% of measurement points, with PE within 10 cm for 12% of measurement

Optics EXPRESS

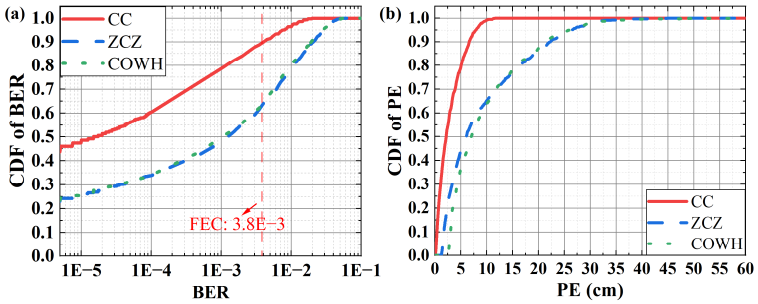

Fig. 11. For syn. w/ NLOS VLCP systems: CDF curve of the (a) BER; and (b) PE, based on different codes, where the pink line in (a) represents the FEC criterion of 3.8E−3.

points. In contrast, the performance of the ZCZ codes is the least favorable, with only about 8% of measurement points achieving a BER below the FEC threshold and 8% of measurement points with PE within the 10-cm range. These results strongly demonstrate that in a complex indoor environment involving asynchronous and continuous bitstream transmission with multipath propagation, the VLCP system based on CC codes effectively mitigates MAI and ISI due to the excellent correlation properties of CC codes, ensuring high levels of communication reliability and positioning accuracy. In contrast, ZCZ codes and COWH codes suffer orthogonality degradation under such conditions, leading to increased mutual interference between VLCP signals, thereby challenging effective communication and accurate positioning services in the VLCP system.

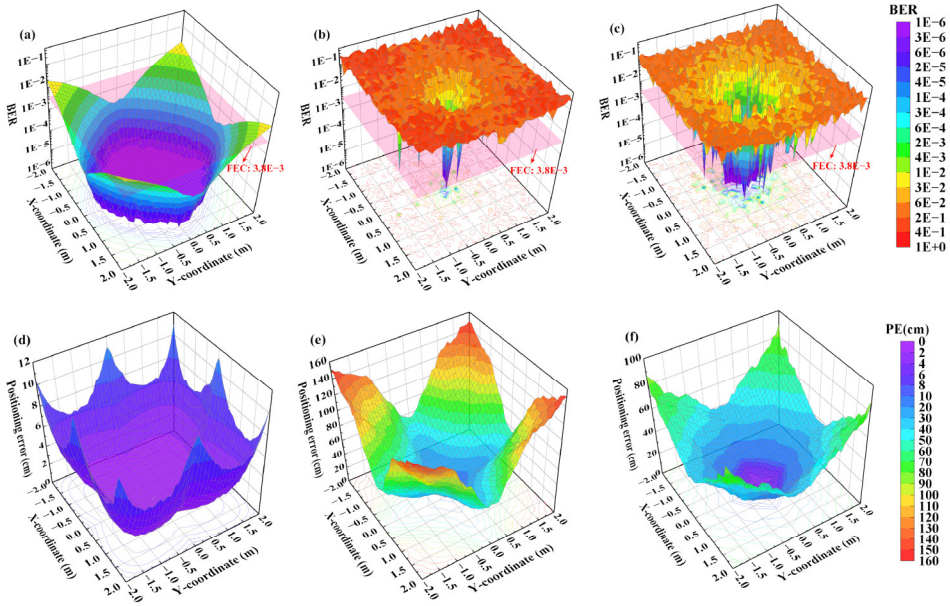

Fig. 12. For asyn. w/ NLOS VLCP systems: Color-mapped surface plots of the BER based on (a) CC codes; (b) ZCZ codes; and (c) COWH codes, where the pink planes represent the FEC criterion of 3.8E−3. Surface plots of the PE based on (d) CC codes; (e) ZCZ codes; and (f) COWH codes.

Finally, we conduct a comprehensive comparison of the performance of three coding schemes under various system settings, with their box plots of BER and PE shown in Fig. 14. It is

Optics EXPRESS

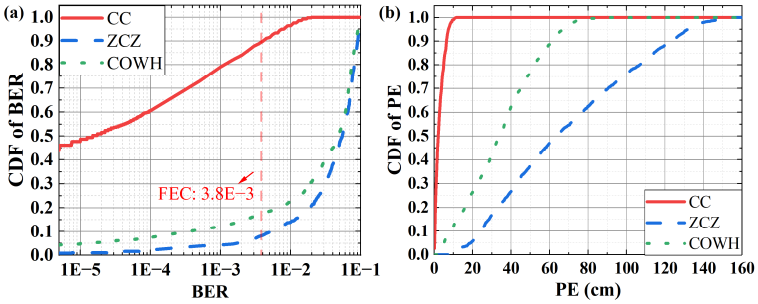

Fig. 13. For asyn. w/ NLOS VLCP systems: CDF curve of the (a) BER; and (b) PE, based on different codes, where the pink line in (a) represents the FEC criterion of 3.8E−3.

evident that CC codes consistently maintain excellent communication quality and positioning accuracy across different system configurations, with minimal variation in BER and PE. The average BER remains below the FEC threshold, and the average PE is consistently less than 3 cm, regardless of the system setting. In contrast, the performance of ZCZ and COWH codes varies significantly with changes in system settings. In the synchronous system without NLOS channels, both schemes achieve similar average BER and PE at 4.9E−3 and 6.6 cm, respectively. However, in the syn. w/ NLOS system, because of the ISI, their performance slightly deteriorates: the average BER and PE for ZCZ codes increase to 5.8E−3 and 9.3 cm, while for COWH codes, they rise to 6.1E−3 and 13.7 cm, respectively. In the asyn. w/o NLOS system, the presence of MAI leads to a more pronounced decline in performance: the average BER and PE for ZCZ codes increase to 1.4E−1 and 68.4 cm, and for COWH codes, they rise to 5.7E−2 and 34.0 cm. Finally, in the asyn. w/ NLOS system, the combined effect of MAI and ISI further degrade performance: the average BER and PE for ZCZ codes increase to 1.4E−1 and 69 cm, and for COWH codes, they rise to 5.8E−2 and 34.6 cm. Thus, in the asynchronous system with both MAI and ISI, our proposed system demonstrates superior performance, reducing the average BER by approximately 99% and 98% and the average PE by about 96% and 92%, compared to ZCZ and COWH codes-based VLCP systems, respectively. In addition, we find that the degradation in positioning performance is more obvious than in communication performance under the influence of MAI and ISI. This is because the noise introduced by MAI and ISI causes deviations in the CV used for RSS calculation, which directly leads to increased positioning errors. However, for the communication function, we recover user data by applying a threshold to CV as shown in Eq. (25), which is more tolerant of errors in the correlation values. Therefore, positioning performance is more adversely affected by MAI and ISI compared to communication performance.

Furthermore, we compare the estimated receiver positions with the actual receiver positions for each coding scheme under different system settings. For clarity, we select measurement points at intervals of 0.5 meters and connect the estimated positions with the actual positions using colored lines, as shown in Fig. 15. The results clearly indicate that the VLCP system based on CC codes accurately localizes the receiver even near the room boundaries, across all system settings. Conversely, the VLCP systems based on ZCZ and COWH codes only provide satisfactory receiver localization in synchronous systems. When the system loses synchronization, these systems can only roughly localize the receiver near the center of the room.

In summary, the proposed MC-OCM scheme based on CC codes employs a multi-carrier and multi-code structure, resulting in higher complexity compared to ZCZ and COWH schemes. But, MC-OCM offers greater coding gain, effectively mitigating the impact of AWGN. Additionally, the superior correlation properties of CC codes significantly reduce the effects of MAI and ISI in

Optics EXPRESS

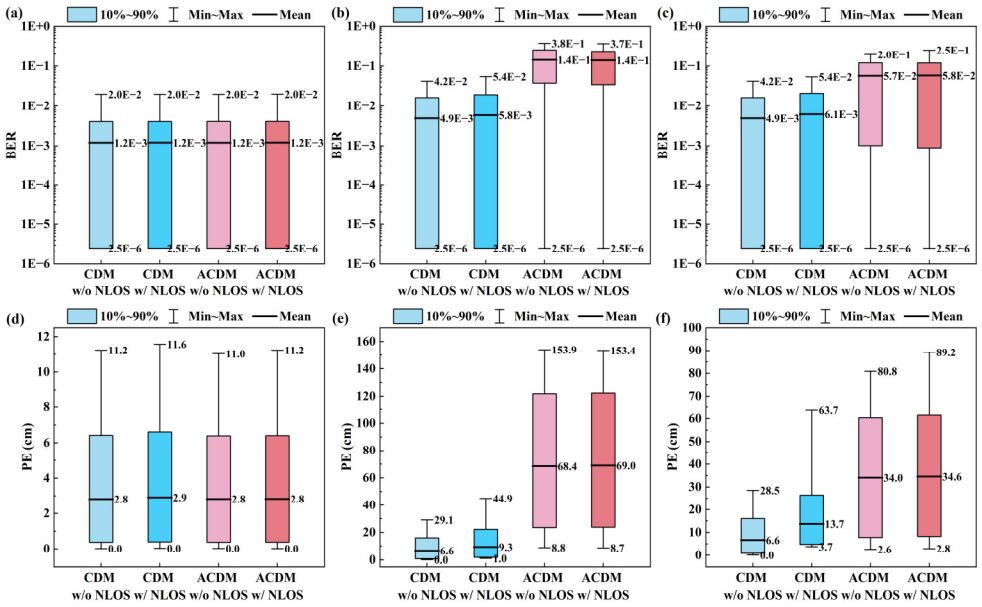

Fig. 14. Box plots of the BER for (a) CC codes; (b) ZCZ codes; and (c) COWH codes, and the PE for (d) CC codes; (e) ZCZ codes; and (f) COWH codes under different system setups.

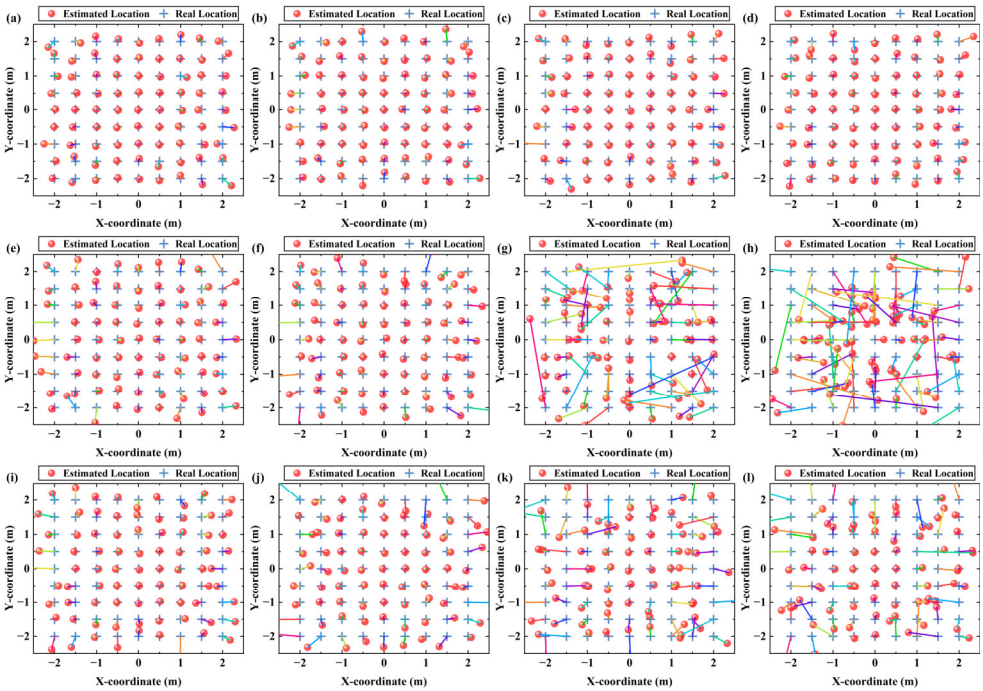

Fig. 15. Comparisons between a part of real locations and estimated locations for the CC codes used in (a) syn. w/o NLOS; (b) syn. w/ NLOS; (c) asyn. w/o NLOS; and (d) asyn. w/ NLOS, for ZCZ codes used in (e) syn. w/o NLOS; (f) syn. w/ NLOS; (g) asyn. w/o NLOS; and (h) asyn. w/ NLOS, and for COWH codes used in (i) syn. w/o NLOS; (j) syn. w/ NLOS; (k) asyn. w/o NLOS; and (l) asyn. w/ NLOS.

Optics EXPRESS

asynchronous systems, leading to substantial decreases in BER and positioning errors. These advantages greatly enhance the system's performance and overall stability.

6. Conclusions

This paper investigated the development and evaluation of an asynchronous VLCP system based on MC-OCM. By leveraging the perfect correlation properties of CC codes, our design overcomes the conventional reliance on system synchronization in CDM-based VLCP systems, achieving MAI and ISI-free transmission in asynchronous scenarios. This enables precise decoding of VLCP signals from different LED transmitters, simultaneously ensuring stable VLC functionality and high-precision VLP capabilities. Theoretical validation and comprehensive simulations across various scenarios, including comparisons with systems based on ZCZ and COWH codes, unequivocally demonstrated the superiority of our system. Compared to ZCZ and COWH codes-based VLCP systems, our proposed system reduces the average BER by approximately 99% and 98% and the average PE by about 96% and 92%, respectively, in challenging scenarios featuring asynchronous and continuous bitstream transmission and multipath propagation. These results confirmed the robustness and effectiveness of our proposed VLCP system in complex asynchronous transmission scenarios. Future research will validate the multi-user capability and effectiveness of the proposed system through practical experiments considering varying reflectivity of surfaces, ambient light conditions and occlusion by objects. Furthermore, we aim to enhance system performance by optimizing parameters like code length, LED emission strength, and LED layout. Lastly, we will explore the integration of intelligent reflective surfaces on walls to control multipath reflections and improve illumination uniformity throughout the room, thereby enhancing communication and positioning quality, especially at the room's edges.

Appendix A. Proof of Eq. (20)

First, by substituting Eq. (16) and Eq. (17) into Eq. (20), and after simplification, we can obtain:

$$
\begin{aligned}
ds_{ijk}(z) &= \sum_{n=T_c(z-1)}^{zT_c-1} R(n) \times 2\cos(2\pi f_j n + \theta_i) \\
&= \sum_{n=T_c(z-1)}^{zT_c-1} \left(\sum_{i=1}^{N} \left\{ \begin{array}{l} P_t \left[\delta S_i \left\langle z + \tau_{\mathrm{LOS}i} \right\rangle + 1\right] h_{\mathrm{LOS}i} + \\ P_t \left[\delta S_i \left\langle z + \tau_{\mathrm{NLOS}i} \right\rangle + 1\right] \int_{\mathrm{walls}} dh_{\mathrm{NLOS}i} \end{array} \right\} + N_{\mathrm{AWGN}}(n) \right) \times 2\cos(2\pi f_j n + \theta_i) \\
&= \gamma P_t \sum_{n=T_c(t-1)}^{tT_c-1} \sum_{i=1}^{N} \left[S_i \left\langle z + \tau_{\mathrm{LOS}i} \right\rangle h_{\mathrm{LOS}i} + S_i \left\langle z + \tau_{\mathrm{NLOS}i} \right\rangle \int_{\mathrm{walls}} dh_{\mathrm{NLOS}i} \right] \times 2\cos(2\pi f_j n + \theta_i) \\
&\quad + \gamma P_t \left(h_{\mathrm{LOS}i} + \int_{\mathrm{walls}} dh_{\mathrm{NLOS}i} \right) \sum_{n=T_c(t-1)}^{tT_c-1} 2\cos(2\pi f_j n + \theta_i) + \sum_{n=T_c(t-1)}^{tT_c-1} N_{\mathrm{AWGN}}(n) \times 2\cos(2\pi f_j n + \theta_i) \\
&= \gamma P_t \sum_{n=T_c(t-1)}^{tT_c-1} \sum_{i=1}^{N} \left[S_i \left\langle z + \tau_{\mathrm{LOS}i} \right\rangle h_{\mathrm{LOS}i} + S_i \left\langle z + \tau_{\mathrm{NLOS}i} \right\rangle \int_{\mathrm{walls}} dh_{\mathrm{NLOS}i} \right] \times 2\cos(2\pi f_j n + \theta_i) + N_{nsij}(z)
\end{aligned}
$$

Optics EXPRESS

We further incorporate Eq. (13)-(15) into the aforementioned equation, yielding:

$$
\begin{aligned}
ds_{ijk}(z) &= \gamma P_t \sum_{n=T_c(z-1)}^{zT_c-1} \sum_{l=1}^{N} \left[S_l \langle z+\tau_{\mathrm{LOS}l} \rangle h_{\mathrm{LOS}l} + S_l \langle z+\tau_{\mathrm{NLOS}l} \rangle \int_{\mathrm{walls}} dh_{\mathrm{NLOS}l} \right] \times 2\cos(2\pi f_j n + \theta_i) + N_{nsij}(z) \\
&= \gamma P_t \delta \sum_{n=T_c(z-1)}^{zT_c-1} \sum_{l=1}^{N} \sum_{m=1}^{M} \left[\begin{array}{l} h_{\mathrm{LOS}l} u_{la} \mathbf{Z}_{lm} \langle z+\tau_{\mathrm{LOS}l} \rangle \cos(2\pi f_m n + \theta_l) + \\ \int_{\mathrm{walls}} dh_{\mathrm{NLOS}l} u_{lb} \mathbf{Z}_{lm} \langle z+\tau_{\mathrm{NLOS}l} \rangle \cos(2\pi f_m n + \theta_l) \end{array} \right] \times 2\cos(2\pi f_j n + \theta_i) + N_{nsij}(z) \\
&= \gamma P_t \delta \sum_{l=1}^{N} \sum_{m=1}^{M} \left(\begin{array}{l} h_{\mathrm{LOS}l} u_{la} \mathbf{Z}_{lm} \langle z+\tau_{\mathrm{LOS}l} \rangle + \\ \int_{\mathrm{walls}} dh_{\mathrm{NLOS}l} u_{lb} \mathbf{Z}_{lm} \langle z+\tau_{\mathrm{NLOS}l} \rangle \end{array} \right) \sum_{n=T_c(z-1)}^{zT_c-1} \cos(2\pi f_m n + \theta_l) \times 2\cos(2\pi f_j n + \theta_i) + N_{nsij}(z) \\
&= \gamma P_t \delta \sum_{l=1}^{N} \left(\begin{array}{l} h_{\mathrm{LOS}l} u_{la} \mathbf{Z}_{lj} \langle z+\tau_{\mathrm{LOS}l} \rangle + \\ \int_{\mathrm{walls}} dh_{\mathrm{NLOS}l} u_{lb} \mathbf{Z}_{lj} \langle z+\tau_{\mathrm{NLOS}l} \rangle \end{array} \right) \sum_{n=T_c(z-1)}^{zT_c-1} \cos(2\pi f_j n + \theta_l) \times 2\cos(2\pi f_j n + \theta_i) \\
&\quad + \gamma P_t \delta \sum_{l=1}^{N} \sum_{\substack{m=1, \\ m\neq j}}^{M} \left(\begin{array}{l} h_{\mathrm{LOS}l} u_{la} \mathbf{Z}_{lm} \langle z+\tau_{\mathrm{LOS}l} \rangle + \\ \int_{\mathrm{walls}} dh_{\mathrm{NLOS}l} u_{lb} \mathbf{Z}_{lm} \langle z+\tau_{\mathrm{NLOS}l} \rangle \end{array} \right) \sum_{n=T_c(z-1)}^{zT_c-1} \cos(2\pi f_m n + \theta_l) \times 2\cos(2\pi f_j n + \theta_i) + N_{nsij}(z)
\end{aligned}
$$

where $\begin{cases} la = l(k-1), & (k-1)L \le z < (k-1)L + \tau_{\mathrm{LOS}i} \\ la = lk, & (k-1)L + \tau_{\mathrm{LOS}i} \le z < kL \end{cases}$,

and $\begin{cases} lb = l(k-1), & (k-1)L \le z < (k-1)L + \tau_{\mathrm{NLOS}i} \\ lb = lk, & (k-1)L + \tau_{\mathrm{NLOS}i} \le z < kL \end{cases}$.

Among the above formula, we can calculate the following results:

$$
\begin{aligned}
&\sum_{n=T_c(z-1)}^{zT_c-1} \cos(2\pi f_m n + \theta_l) \times 2\cos(2\pi f_j n + \theta_i) \\
&= 2 \sum_{n=T_c(z-1)}^{zT_c-1} \frac{1}{2} \{ \cos[2\pi(f_m + f_j)n + (\theta_l + \theta_i)] + \cos[2\pi(f_m - f_j)n + (\theta_l - \theta_i)] \} \\
&= \sum_{n=T_c(z-1)}^{zT_c-1} \{ \cos[2\pi(f_m + f_j)n + (\theta_l + \theta_i)] + \cos[2\pi(f_m - f_j)n + (\theta_l - \theta_i)] \} \\
&= \begin{cases} 1 + \cos(\theta_l - \theta_i) & m = j \\ 0 & m \neq j \end{cases}.
\end{aligned}
$$

Then, by substituting these results into the aforementioned formula, we arrive at:

$$
ds_{ijk}(z) = \gamma P_t \delta \sum_{l=1}^{N} \left[h_{\mathrm{LOS}l} u_{la} \mathbf{Z}_{lj} \langle z+\tau_{\mathrm{LOS}l} \rangle + \int_{\mathrm{walls}} dh_{\mathrm{NLOS}l} u_{lb} \mathbf{Z}_{lj} \langle z+\tau_{\mathrm{NLOS}l} \rangle \right] (1 + \varpi_l) + N_{nsij}(z),
$$

where $\varpi_l = \cos(\theta_l - \theta_i)$,

$$
\begin{cases} la = l(k-1), & (k-1)L \le z < (k-1)L + \tau_{\mathrm{LOS}i} \\ la = lk, & (k-1)L + \tau_{\mathrm{LOS}i} \le z < kL \end{cases},
$$

$$
\begin{cases} lb = l(k-1), & (k-1)L \le z < (k-1)L + \tau_{\mathrm{NLOS}i} \\ lb = lk, & (k-1)L + \tau_{\mathrm{NLOS}i} \le z < kL \end{cases},
$$

and $N_{nsij}(z) = \sum_{n=T_c(z-1)}^{zT_c-1} N_{\mathrm{AWGN}}(n) \times 2\cos(2\pi f_j n + \theta_i)$.

Thus, Eq. (20) is proven.

Optics EXPRESS

Appendix B. Proof of Eq. (22)

First, we substitute Eq. (21) into Eq. (22) to obtain:

$$
\begin{aligned}
&\Im_{ik} = \tfrac{1}{M}\sum_{j=1}^{M} de_{ijk} \\
&= \gamma P_t \delta \tfrac{1}{LM}\Bigg\{ h_{\mathrm{LOS}i}\sum_{j=1}^{M}\sum_{n=0}^{L-1} u_k \boldsymbol{Z}_{ij}(n)\boldsymbol{Z}_{ij}(n) \\
&+ \int_{\mathrm{walls}} dh_{\mathrm{NLOS}i}\left[\sum_{j=1}^{M}\sum_{n=0}^{\tilde{\tau}_{\mathrm{NLOS}i}-1} u_{i(k-1)}\boldsymbol{Z}_{ij}\left\langle n+\tilde{\tau}_{\mathrm{NLOS}i}\right\rangle \boldsymbol{Z}_{ij}(n) + \sum_{j=1}^{M}\sum_{n=\tilde{\tau}_{\mathrm{NLOS}i}}^{L-1} u_{ik}\boldsymbol{Z}_{ij}\left\langle n+\tilde{\tau}_{\mathrm{NLOS}i}\right\rangle \boldsymbol{Z}_{ij}(n)\right] \\
&+ \sum_{\substack{l=1,\\ l\neq i}}^{N} h_{\mathrm{LOS}l}\left[\sum_{j=1}^{M}\sum_{n=0}^{\tilde{\tau}_{\mathrm{LOS}l}-1} u_{l(k-1)}\boldsymbol{Z}_{lj}\left\langle n+\tilde{\tau}_{\mathrm{LOS}l}\right\rangle \boldsymbol{Z}_{ij}(n) + \sum_{j=1}^{M}\sum_{n=\tilde{\tau}_{\mathrm{LOS}l}}^{L-1} u_{lk}\boldsymbol{Z}_{lj}\left\langle n+\tilde{\tau}_{\mathrm{LOS}l}\right\rangle \boldsymbol{Z}_{ij}(n)\right](1+\varpi_l) \\
&+ \sum_{\substack{l=1,\\ l\neq i}}^{N} \int_{\mathrm{walls}} dh_{\mathrm{NLOS}l}\left[\sum_{j=1}^{M}\sum_{n=0}^{\tilde{\tau}_{\mathrm{NLOS}l}-1} u_{l(k-1)}\boldsymbol{Z}_{lj}\left\langle n+\tilde{\tau}_{\mathrm{NLOS}l}\right\rangle \boldsymbol{Z}_{ij}(n) + \sum_{j=1}^{M}\sum_{n=\tilde{\tau}_{\mathrm{NLOS}l}}^{L-1} u_{lk}\boldsymbol{Z}_{lj}\left\langle n+\tilde{\tau}_{\mathrm{NLOS}l}\right\rangle \boldsymbol{Z}_{ij}(n)\right](1+\varpi_l)\Bigg\} \\
&+ \tfrac{1}{ML}\sum_{j=1}^{M}\sum_{n=0}^{L-1} N_{nsij}(n)\times \boldsymbol{Z}_{ij}(n)
\end{aligned}
\tag{.}
$$

Then, by introducing Eq. (11) and Eq. (12) into the above equation, we arrive at the final result:

$$
\begin{aligned}
&\Im_{ik} = \gamma P_t \delta h_{\mathrm{LOS}i} u_k \rho(\boldsymbol{Z}_i, \boldsymbol{Z}_i; 0) \\
&+\gamma P_t \delta \int_{\mathrm{walls}} dh_{\mathrm{NLOS}i}[u_{i(k-1)}\sigma(\boldsymbol{Z}_i, \boldsymbol{Z}_i; \tilde{\tau}_{\mathrm{NLOS}i}) + u_{ik}\sigma(\boldsymbol{Z}_i, \boldsymbol{Z}_i; L-\tilde{\tau}_{\mathrm{NLOS}i})] \\
&+\gamma P_t \delta \left\{ \begin{array}{l} \sum\limits_{\substack{l=1,\\ l\neq i}}^{N} h_{\mathrm{LOS}l}[u_{l(k-1)}\sigma(\boldsymbol{Z}_i, \boldsymbol{Z}_l; \tilde{\tau}_{\mathrm{LOS}l}) + u_{lk}\sigma(\boldsymbol{Z}_i, \boldsymbol{Z}_l; L-\tilde{\tau}_{\mathrm{LOS}l})](1+\varpi_l) + \\ \sum\limits_{\substack{l=1,\\ l\neq i}}^{N} \int_{\mathrm{walls}} dh_{\mathrm{NLOS}l} \left[\begin{array}{l} u_{l(k-1)}\sigma(\boldsymbol{Z}_i, \boldsymbol{Z}_l; \tilde{\tau}_{\mathrm{NLOS}l}) + \\ u_{lk}\sigma(\boldsymbol{Z}_i, \boldsymbol{Z}_l; L-\tilde{\tau}_{\mathrm{NLOS}l}) \end{array} \right](1+\varpi_l) \end{array} \right\}. \\
&+\tfrac{1}{ML}\sum_{j=1}^{M}\sum_{n=0}^{L-1} N_{nsij}(n)\times \boldsymbol{Z}_{ij}(n) \\
&= \gamma P_t \delta h_{\mathrm{LOS}i} u_k \rho(\boldsymbol{Z}_i, \boldsymbol{Z}_i; 0) + ISI + MAI + AWGN
\end{aligned}
$$

Thus, Eq. (22) is proven.

Funding. Key Laboratory in Science and Technology Development Project of Suzhou (SYG202112); Hong Kong Research Grants Council (15212720); National Natural Science Foundation of China (62001319); Open Fund of IPOC Beijing University of Posts and Telecommunications (BUPT) (IPOC2020A009).

Disclosures. The authors declare no conflicts of interest.

Data availability. Data underlying the results presented in this paper are not publicly available at this time but may be obtained from the authors upon reasonable request.

References

1. S. Dang, O. Amin, B. Shihada, *et al.*, "What should 6 G be?" Nat. Electron. **3**(1), 20–29 (2020).
2. X. You, C.-X. Wang, J. Huang, *et al.*, "Towards 6 G wireless communication networks: vision, enabling technologies, and new paradigm shifts," Sci. China Inf. Sci. **64**(1), 110301 (2021).
3. D. C. Nguyen, M. Ding, P. N. Pathirana, *et al.*, "6 G Internet of Things: A comprehensive survey," IEEE Internet Things J. **9**(1), 359–383 (2021).
4. N. Chi, Y. Zhou, Y. Wei, *et al.*, "Visible light communication in 6G: Advances, challenges, and prospects," IEEE Veh. Technol. Mag. **15**(4), 93–102 (2020).
5. Y. Zhuang, L. Hua, L. Qi, *et al.*, "A survey of positioning systems using visible LED lights," IEEE Commun. Surveys Tuts. **20**(3), 1963–1988 (2018).
6. C. Liang, J. Li, S. Liu, *et al.*, "Integrated sensing, lighting and communication based on visible light communication: A review," Digital Signal Process. **145**, 104340 (2024).
7. C. Yu, X. You, Z. Liu, *et al.*, "Conceptual design for indoor visible light communication and positioning cooperative systems," in *2020 22nd International Conference on Transparent Optical Networks (ICTON)* (IEEE, 2020), pp. 1–4.

Optics EXPRESS

8. M. Afzalan and F. Jazizadeh, "Indoor positioning based on visible light communication," ACM Computing Surveys **52**(2), 1–36 (2020).
9. P. Du, S. Zhang, C. Chen, *et al.*, "Experimental demonstration of 3D visible light positioning using received signal strength with low-complexity trilateration assisted by deep learning technique," IEEE Access **7**, 93986–93997 (2019).
10. X. Zhang, J. Duan, Y. Fu, *et al.*, "Theoretical accuracy analysis of indoor visible light communication positioning system based on received signal strength indicator," J. Lightwave Technol. **32**(21), 4180–4186 (2014).
11. Y. Zhang, Z. Wei, Z. Liu, *et al.*, "Optical communication and positioning convergence for flexible underwater wireless sensor network," J. Lightwave. Technol. **41**(16), 5321–5327 (2023).
12. S. Ma, R. Yang, B. Li, *et al.*, "Optimal power allocation for integrated visible light positioning and communication system with a single LED-Lamp," IEEE Trans. Commun. **70**(10), 6734–6747 (2022).
13. X. Lin and L. Zhang, "Intelligent and practical deep learning aided positioning design for visible light communication receivers," IEEE Commun. Lett. **24**(3), 577–580 (2020).
14. M. Nassiri, G. Baghersalimi, and Z. Ghassemlooy, "A hybrid VLP and VLC system using m-CAP modulation and fingerprinting algorithm," Opt. Commun. **473**, 125699 (2020).
15. H. Yang, W.-D. Zhong, C. Chen, *et al.*, "Integration of visible light communication and positioning within 5 G networks for internet of things," IEEE Network **34**(5), 134–140 (2020).
16. H. Yang, S. Zhang, A. Alphones, *et al.*, "An advanced integrated visible light communication and localization system," IEEE Trans. Commun. **71**(12), 7149–7162 (2023).
17. T. Wei, S. Liu, and X. Du, "Visible light integrated positioning and communication: a multi-task federated learning framework," IEEE Trans. Mobile Comput. **22**(12), 7086–7103 (2023).
18. S. Zhang, P. Du, H. Yang, *et al.*, "Recent progress in visible light positioning and communication systems," Ieice Trans. Commun. **E106.B**(2), 84–100 (2023).
19. H. Yang, C. Chen, W.-D. Zhong, *et al.*, "Demonstration of a quasi-gapless integrated visible light communication and positioning system," IEEE Photonics Technol. Lett. **30**(23), 2001–2004 (2018).
20. D. Chen, K. Fan, J. Wang, *et al.*, "Integrated visible light communication and positioning CDMA system employing modified ZCZ and Walsh code," Opt. Express **30**(22), 40455–40469 (2022).
21. Z. Liu and C. Yu, "Multi-user visible light communication and positioning system based on dual-domain multiplexing scheme," Photonics **10**(3), 306 (2023).
22. H. Mrabet, A. Cherifi, T. Raddo, *et al.*, "A Comparative study of asynchronous and synchronous OCDMA Systems," IEEE Syst. J. **15**(3), 3642–3653 (2021).
23. D. Chen, Q. Wang, J. Wang, *et al.*, "Performance evaluation of ZCC and OZCZ code set in an integrated VLCP-CDMA System," IEEE Photonics Technol. Lett. **34**(16), 846–849 (2022).
24. O. González, J. A. Martín-González, M. F. Guerra-Medina, *et al.*, "Cyclic code-shift extension keying for multi-user optical wireless communications," Electron. Lett. **51**(11), 847–849 (2015).
25. Y. Qiu, H.-H. Chen, J. Li, *et al.*, "VLC-CDMA systems based on optical complementary codes," IEEE Wireless Commun. **27**(1), 147–153 (2020).
26. Á. De-La-Llana-Calvo, J.-L. Lázaro-Galilea, A. Gardel-Vicente, *et al.*, "Analysis of multiple-access discrimination techniques for the development of a PSD-based VLP system," Sensors **20**(6), 1717 (2020).
27. H. Chen, W. Guan, S. Li, *et al.*, "Indoor high precision three-dimensional positioning system based on visible light communication using modified genetic algorithm," Opt. Commun. **413**, 103–120 (2018).
28. F. Miramirkhani and M. Uysal, "Channel Modeling and Characterization for Visible Light Communications," IEEE Photonics. J. **7**(6), 1–16 (2015).
29. S. De Lausnay, L. De Strycker, J.-P. Goemaere, *et al.*, "Influence of MAI in a CDMA VLP system," in *2015 International Conference on Indoor Positioning and Indoor Navigation (IPIN)* (IEEE, 2015), pp. 1–9.
30. A. Tawfiq, J. Abouei, and K. N. Plataniotis, "Cyclic orthogonal codes in CDMA-based asynchronous wireless body area networks," in *2012 IEEE International Conference on Acoustics, Speech and Signal Processing (ICASSP)* (IEEE, 2012), pp. 1593–1596.
31. H. H. Chen, D. Hank, M. E. Maganaz, *et al.*, "Design of next-generation cdma using orthogonal complementary codes and offset stacked spreading," IEEE Wireless Commun. **14**(3), 61–69 (2007).
32. H.-H. Chen and J.-F. Yeh, "A complementary codes-based CDMA architecture for wideband mobile internet with high spectral efficiency and exact rate matching," Int. J. Commun. Syst. **16**(6), 497–512 (2003).
33. Z. Wang, W.-D. Zhong, C. Yu, *et al.*, "Performance of dimming control scheme in visible light communication system," Opt. Express **20**(17), 18861–18868 (2012).
34. T. Komine and M. Nakagawa, "Fundamental analysis for visible-light communication system using LED lights," IEEE Trans. Consumer Electron. **50**(1), 100–107 (2004).

158.132.161.52 2025-04-03 21:01:11